Icarus 227 (2014) 132–151

Contents lists available at ScienceDirect

Icarus

journal homepage: www.elsevier.com/locate/icarus

Lunar mare basalts in the Aristarchus region: Implications for the stratigraphic sequence from Clementine UVVIS data

F. Zhang [a,b], Y.L. Zou [a,*], Y.C. Zheng [a,c,d,*], X.H. Fu [a], Y.C. Zhu [a,b]

[a] National Astronomical Observatories, Chinese Academy of Sciences, Beijing 100012, China
[b] University of Chinese Academy of Sciences, Beijing 100049, China
[c] Center for Space Science Research, The Hong Kong University of Science and Technology, Hong Kong, China
[d] Space Science Institute, Macau University of Science and Technology, Macau, China

ARTICLE INFO

Article history:
Received 1 June 2012
Revised 13 September 2013
Accepted 13 September 2013
Available online 25 September 2013

Keywords:
Spectroscopy
Mineralogy
Volcanism
Moon, surface

ABSTRACT

The Aristarchus region of Oceanus Procellarum is an area concentrated with lunar basalts, which were mainly produced by the last major phase of lunar volcanism on the western nearside. A group of lunar sample and remote sensing scientists have carried out the extensive task of characterization of lunar mare soils with regard to their mineralogical and chemical makeup and regional geologic mapping. Spectral parameters of the high spatial resolution Clementine images are used to identify and define these basalts as different compositional and spectral units. This endeavor is aimed at deciphering the subtle spectral characteristics of mare soils and validating the mapping technique used in this study, together with making statistical analysis of the links between the basalt types with ages in order to provide a further understanding of material types and geologic evolution in the Aristarchus region of the Moon. From the new perspective of mining geologic information in multivariable image-spaces, spectrally distinct 9 high-Ti and 11 low-Ti basalt reference spectra have been distinguished and as a result, more than 70 spectrally and compositionally basaltic units, which range in age from 1.20 b.y. to 3.74 b.y., have been identified. To some extent, a potential relationship between composition and relative age exists in the statistical analysis of the links between spectral types (related with the Clementine ratio colors) of various basalts and ages in this study, which suggests that composition with different states of maturity correlate with age to some extent. The mineralogical characteristics and spectra-age relationship in the Marius Hills region indicate that the early basalts may still be exposed at the surface deposit after prolonged volcanic activity in this region. This may be a result of not being blanketed by later lava flows, or lava extrusions of underlying low-Ti basalts. In addition, stratigraphic analysis also reveals and confirms that TiO_2 concentrations appear to vary independently with time, and generally eruptions of TiO_2-rich and TiO_2-poor basalts have occurred contemporaneously.

© 2013 Elsevier Inc. All rights reserved.

1. Introduction

In recent years, there has been an increasing interest in lunar mare basalts with a large volume of imagery data having been achieved by a series of lunar exploration. According to our present knowledge of the Moon, the relatively smooth and dark lunar mare basalts cover about 17% of the lunar surface and are thought to make up about 1% of the total volume of the lunar crust (Head, 1976). Most of our knowledge of the lunar interior comes from studies of mare basalts. Previous experimental studies of mare basalt compositions suggest that the lunar basalts were produced by partial melting of mafic sources within the lunar mantle at depths of <550 km (Lofgren et al., 1981; Longhi, 1992; Wieczorek and Phillips, 2000). These sources are generally thought to be the cumulate rocks produced during the early differentiation of the Moon. Basin-associated eruption of mare basalts occurred during and following the late stages of catastrophic bombardment. This volcanic activity was possibly an extension of the thermal event that initiated pre-basin volcanism (Shearer and Papike, 1999) though the high abundance of heat-producing elements (the KREEP component) in the underlying lunar mantle most likely served as a thermal driver for the prolonged volcanic activity in some local regions (e.g., the Aristarchus region, Hagerty et al., 2009). The heat source for remelting cumulates to form the late basaltic outpourings remains incompletely understood and presents challenging problems for current researchers (Grove and Krawczynski, 2009).

Our knowledge of mare basalt types beyond those sampled at the Apollo and Luna landing sites has been widely extended by remote studies of the lunar surface (e.g., Pieters, 1977, 1978; Pieters et al., 1980; Whitford-Stark and Head, 1980; Hiesinger et al., 2000,

* Corresponding author at: National Astronomical Observatories, Chinese Academy of Sciences, Beijing 100012, China.
E-mail addresses: fzhang@nao.cas.cn, ylzou@nao.cas.cn (Y.L. Zou), zyc@nao.cas.cn (Y.C. Zheng).

0019-1035/$ - see front matter © 2013 Elsevier Inc. All rights reserved.
http://dx.doi.org/10.1016/j.icarus.2013.09.011

2003; Staid and Pieters, 2000; Heather and Dunkin, 2002; Kodama and Yamaguchi, 2003; Bugiolacchi and Guest, 2008). Such studies suggest that mare basalts retain a record of recent impact cratering and a wide range of volcanic processes, and the studies on mare basalts are important for us to understand lunar volcanic activities. Therefore, it is necessary to properly characterize lunar mare basalt compositions, which serve as probes of the interior composition of the Moon (Giguere et al., 2000). Mapping homogeneous basalt units is important, and a crucial prerequisite for further compositional (chemical and physical) and volcanic evolution investigations for the Moon. In previous studies related to mapping basalt units, two methods have been widely used to investigate and classify different mare basalt units on the Moon: one is by TiO_2 contents (chemical property) (e.g., Papike et al., 1976; Johnson et al., 1977b, 1991; Davis, 1980; Neal and Taylor, 1992; Pieters et al., 1993; Melendrez et al., 1994; Giguere et al., 2000; Le Bas, 2001), and the other is spectral mapping (e.g., Pieters, 1978; Pieters et al., 1980, 1995; Robinson et al., 1992; Belton et al., 1992; Greeley et al., 1993; Williams et al., 1995; Hiesinger et al., 1996, 2000, 2003, 2008; Heather et al., 1999; Kodama and Yamaguchi, 2003, 2005).

The aim of this study was to evaluate and validate our new systematic approach to comprehensively make use of Clementine UVVIS data to classify basalt units and make statistical analysis on the links between basalt types and ages. Spectral types not only provide compositional information, but also the exposure age of the units, which is caused by space weathering. We expect this investigation will provide a further understanding of material types and geologic evolution on the surface of the Aristarchus region of the Moon. This initial study of lunar basalts focuses on using Clementine UVVIS data. The approach in this study will later be expanded to include using higher spatial and spectral resolution M^3 (Moon Mineralogy Mapper) data. The detailed information of M^3 data and M^3 imaging spectrometer, a guest instrument on India's Chandrayaan-1 mission, can be found in previous studies (Green et al., 2011; Boardman et al., 2011).

2. Background

2.1. Geologic setting of the Aristarchus region

We focused our attention on an area of the lunar surface form 6.57°N to 43.13°N latitude and longitude from 29.54°W to 67.5°W (Fig. 1). The Aristarchus region is one of the most geologically complex areas on the Moon and exposes a variety of spectral, geochemical, radar, and thermal anomalies (e.g., Gorenstein and Bjorkholm, 1973; Zisk et al., 1977; McEwen et al., 1994). Rümker Hills, Aristarchus Plateau Mountains, and Marius Hills region are the three major volcanic complexes (Whitford-Stark and Head, 1977), which have long been recognized in this region of the Oceanus Procellarum on the Moon. The Aristarchus Plateau is a rectangular elevated crustal block about 170 × 220 km that is surrounded by younger mare basalts from Oceanus Procellarum, and is tilted generally westward, sloping away from the Imbrium basin on complex materials from the Imbrium impact event (Chevrel et al., 2009). The geologic and compositional diversity of the Aristarchus region and evidence for active emission of volatiles from Aristarchus crater (Cameron, 1972; Gorenstein and Bjorkholm, 1973) have led to proposals for surface exploration and resource exploitation (e.g., Cintala et al., 1985).

In the study area, various Procellarum basalts have model ages ranging from ~1.2 b.y. to ~3.74 b.y. (Hiesinger et al., 2003). The youngest basalts located in the vicinity of the Aristarchus Plateau are measured at ~1.2 b.y. old (Hiesinger et al., 2008). The crystallization age of the youngest unit in the Marius Hills region is expected to have an age of 1–2 b.y., depending on the details of the impact flux history (Soderblom and Lebofsky, 1972). The study on the Aristarchus pyroclastic glass deposits (Hagerty et al., 2009), which found the source region contained an abundance of Th and other heat-producing elements, suggested that the high abundance of heat-producing elements in the underlying lunar mantle most likely served as a thermal driver for the prolonged volcanic activity in this region of the Moon. In particular, the Aristarchus and Marius complexes are considered as the sources for much of the central Procellarum mare fill (Whitford-Stark and Head, 1977). The reader is referred to (Hackman, 1962; Moore, 1965, 1967; McCauley, 1967; Schaber, 1969; Scott and Eggleton, 1973; Mustard et al., 2011; Staid et al., 2011) for detailed geologic descriptions of this area.

2.2. Previous work

Geological mapping for some regions of the Moon were previously carried out by several authors (e.g., Holt, 1974; Lucchitta, 1978; McCauley, 1967, 1973; Scott et al., 1977; Titley, 1967; Wilhelms and McCauley, 1971; Wilhelms, 1987). Geologic mapping of the maria in the Aristarchus region (Wilhelms and McCauley, 1971) shows a sequence of Imbrian (~3.2–3.5 b.y. ago) and Eratosthenian (~3.2–1.1 b.y.) mare basalts. The definitions of units in this mapping work were based mainly on albedo, morphology and qualitative crater densities on telescopic and Lunar Orbiter images. Based on morphology, spectral reflectance, and other remote sensing information, Whitford-Stark and Head (1980) classified these basalts in the Aristarchus region into three Formations: Telemann Formation, Hermann Formation and Sharp Formation. The Telemann Formation represents the oldest basalt, and is mainly distributed northeast of the Aristarchus Plateau. The Sharp Formation is interpreted as the youngest basalt, which includes nearly the entire high-Ti basalt groups. Flamsteed Basalt, Kunowsky Basalt, Roris Basalt, and Schiaparelli Basalts (the nomenclature used in the work of Whitford-Stark and Head, 1980) belong to the Sharp Formation, of which the age is 2.7 ± 0.7 b.y. Delisle Basalt, Marius Basalt, and Lavoisier Basalt are divisions of the Hermann Formation, the age of which is 3.3 ± 0.3 b.y. Dechen Basalt, Aristarchus Basalt and Dark mantle materials are the Telemann Formation, which is 3.6 ± 0.2 b.y. years old. The ages in the work of Whitford-Stark and Head (1980) are measured by Boyce and Jonnson (1978) from crater degradation/density data. However, these maps are not detailed enough to ensure precise delineation of the investigated basalts (Hiesinger et al., 2003).

Telescopic mapping of four compositionally sensitive spectral parameters (variations in continuum slope (related to titanium content) in the ultraviolet (UV) and visible (VIS), albedo, 1 μm band strength, and 2 μm band strength) have been used to define 13 mare basalt types and 3 additional lunar volcanic groups (Pieters, 1978). Such works have established the distribution of volcanic materials across the lunar nearside and suggest that the majority of observed basalts are not represented in the returned samples. Lunar spectral types were first summarized in previous telescopic studies (McCord et al., 1972a, 1972b; Pieters, 1978). Pieters classified the western high-Ti basalts (basalts in Oceanus Procellarum and Mare Imbrium) into two spectral types (HDSA and hDSA). These are distinct from the Apollo 11 high-Ti sample class (HDWA), which occur primarily within Mare Tranquillitatis. The western high titanium flows cover older mare units within the Imbrium basin and the eastern portion of Oceanus Procellarum. Although the telescopic measurements have high-spectral resolution that allows detailed assessments of mineralogy, only major spatial variations in composition can be detected with these spectra because they have low spatial resolution and represent areas 2–10 km in diameter (Tompkins and Pieters, 1999). Therefore, telescopic spectral

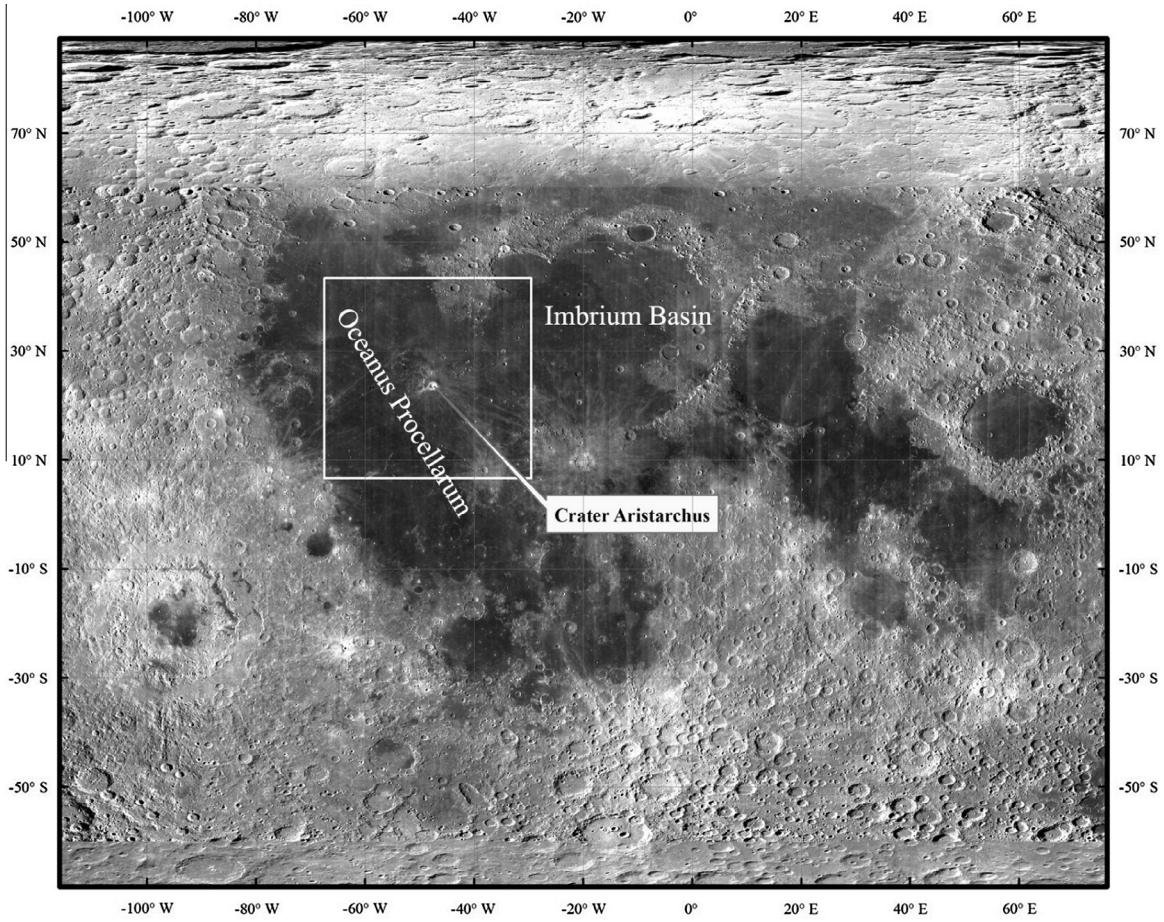


Fig. 1. Part of the nearside of the Moon as seen in LRO WAC USGS global mosaic: the white box indicates the Aristarchus quadrangle region in this study. The simple cylindrical map projection is used.

mapping could not further subdivide mare basalts into different sub-types.

Spectral mapping using today's remote sensing imagery data with higher spatial resolution are used to further refine basalts types in more detail (e.g., Hiesinger et al., 2000, 2003; Staid et al., 2011; Staid and Besse, 2013). Regional spectral differences mapped using spectral ratios have already been used to approximate relatively distinct mare units with homogeneous surface materials (Whitaker, 1972; McCord et al., 1976; Johnson et al., 1977a, 1977b; Pieters, 1978; Whitford-Stark and Head, 1980; Head et al., 1993). Pieters' classification of mare soils was extended to include farside basalts through studies of Mariner 10 multispectral images (Robinson et al., 1992), the interpretation of Galileo solid-state imaging (SSI) multispectral data (Belton et al., 1992; Greeley et al., 1993; Williams et al., 1995), Clementine data (Pieters et al., 1995; Hiesinger et al., 1996, 2003), and recent M^3 data (Besse et al., 2011; Staid et al., 2011; Staid and Besse, 2013). Moreover, Clementine UVVIS 5 band images, together with FeO, TiO_2 content maps, and maturity data derived from Clementine, were used to map boundaries of mare units (e.g., Heather et al., 1999; Kodama and Yamaguchi, 2003, 2005; Kramer et al., 2008a, 2008b).

Lunar sample analysis reveals that TiO_2 contents of mare basalts vary from several tenths of weight percent to ~13 wt% (e.g., BVSP, 1981; Taylor et al., 1991; Neal and Taylor, 1992), and thus titanium concentration became a useful chemical property for classifying lunar mare basalts. The "High-Ti basalts" (>9 wt% TiO_2), "low-Ti basalts" (1.5–9 wt% TiO_2), and "very-low-Ti basalts" (<1.5 wt% TiO_2) in the compositional classification system was once used for Apollo and Luna basalts (e.g., Papike et al., 1998).

However, the statistically small sample data that was obtained by the six Apollo and three Luna missions shows a strongly bimodal distribution of TiO_2 concentrations (e.g., BVSP, 1981; Neal and Taylor, 1992; Papike et al., 1998), and does not reflect the range in TiO_2 abundance of the mare basalts on the surface of the global Moon (Giguere et al., 2000). Thus early comprehensive mapping using remotely sensed data has carried out much work to estimate TiO_2 contents. The first successful Ti derivation and mapping in mare soils via the correlation of the slope of the spectral curve between 0.402 and 0.564 μm and TiO_2 abundance were carried out in the work of Charette et al. (1974). The relatively accurate approach to determine FeO and TiO_2 contents remotely used Clementine UVVIS data, which have the highest spatial resolution established at present (Blewett et al., 1997; Lucey et al., 2000a; Gillis and Jolliff, 2003). Remotely sensed data of nearside mare basalts indicate a unimodal continuum of TiO_2 concentrations (Giguere et al., 2000). However, it is not possible to relate the high-, low-, and very low titanium basalts through low-pressure fractionation schemes (Lofgren et al., 1981; Longhi, 1992; Papike et al., 1998).

3. Approach and definition of units

3.1. Data and processing

The Clementine spacecraft mission (Nozette et al., 1994; McEwen and Robinson, 1997) mapped the Moon during the first half of 1994 using a number of scientific instruments including a UVVIS camera. Clementine's UVVIS data contained five bands centered at

415, 750, 900, 950, and 1000 nm, with an average resolution of 200 m/pixel. The wavelength positions of these camera filters were chosen to maximize the mineralogic information within this spectral region by characterizing the UV/VIS slope and the strength and shape of the 1000 nm ferrous absorption band (e.g., McCord and Johnson, 1970; Burns, 1993).

In this study, in order to investigate the compositional variations and understand the volcanic history of this region, an array of Clementine and Clementine-derived data were used to classify mare basalt units. These include: the Clementine false color band ratio image (R = 750/415 nm; G = 750/950 nm; B = 415/750 nm), 750 nm albedo, 1 μm absorption signatures (1000/750 nm ratio data), and Clementine-derived FeO and TiO_2 content maps (Lucey et al., 2000a). The calibration procedures used on the UVVIS camera image can be found in previous researches (e.g., McEwen and Robinson, 1997; Tompkins and Pieters, 1999). The data were processed at a resolution of 200 m/pixel using the ENVI software program. In the Clementine false color image, a mature low-Ti basalt or mature highland materials appears red, while a mature high-Ti mare basalt or immature highland appears blue. And immature high-Ti basalts will appear bluer than more mature ones. Green, cyan, and yellow indicate freshly exposed basalt (e.g., Heather and Dunkin, 2002; Kodama and Yamaguchi, 2003). The more detailed description of these data sets can also be found in previous studies (e.g., Pieters et al., 1994; McEwen et al., 1994; Belton et al., 1994; Giguere et al., 2000; Staid and Pieters, 2000; Heather and Dunkin, 2002; Zhang et al., 2012).

3.2. Identification of basalt units

Prior to commencing the study, we created a TiO_2 content map (Fig. 2) from Clementine UVVIS data, which was obtained by using the techniques developed by Lucey et al. (2000a). In these Clementine chemical abundance-maps, the FeO and TiO_2 contents are estimated to accuracies of 1 wt% (Lucey et al., 2000a). In addition, the abundance of these elements can also provide a convenient method of mapping and classifying the geologic units (e.g., Kodama and Yamaguchi, 2003). We categorized mare units into three classes based on their TiO_2 content (Le Bas, 2001) as follows: "very low" as a commonly used designation for values <1.5 wt% TiO_2, "low" for the range of 1.5–6 wt% TiO_2, and "high" for the range >6 wt% TiO_2. From Fig. 2, we can see that the mare basalts west and southwest of the Aristarchus Plateau are dominated by high-Ti basalt, while the mare basalts in the northeast, southeast, and northwest of the study region are dominated by low-Ti basalt.

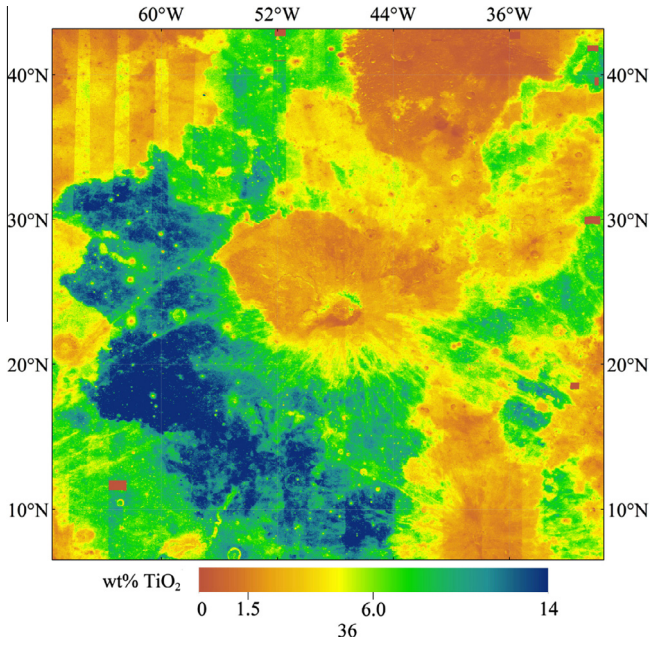


Fig. 2. TiO_2 abundance map of the Aristarchus region, constructed using algorithm of Lucey et al. (2000a). Blue and green color represent >6.0 wt% TiO_2 mare materials. Yellow and orange color indicate mare soils of which TiO_2 content is between 1.5 and 6.0 wt%, and red color shows <1.5 wt% mare soils and non-mare terrains. (For interpretation of the references to color in this figure legend, the reader is referred to the web version of this article.)

On the Moon, impact gardening and space weathering result in compositional mixing and contamination of lunar mare soils with highlands materials (Fig. 3a and b). In the 750 nm reflectance versus 1000/750 nm ratio scatterplot (Fig. 3c), mature and immature lunar soils can be segregated by using spectral scatterplots (Staid and Pieters, 2001). Materials that represent the most immature materials within each mare unit can be selected by identifying pixels that corresponded to the lower right limit of each mare unit's 1.0/0.75 μm ratio versus 0.75 μm scatterplot cloud (purple color in Fig. 3c and d). However, mature mare soils (red color in Fig. 3c and d) can be recognized in the upper left corner of the scatterplot. Then spectral endmembers of unique, spatially coherent units can be identified, and these representative pixels are selected as regions of interest (ROIs) (Fig. 4). The mature mare soils selected and outlined by these ROIs contain the surface and subsurface basalt materials excavated by craters, which cannot be excluded in this way.

The compositional end-members are well represented as approximately pure components on the surface (Mustard and Head, 1996). Therefore, we tried to obtain the relatively pure end-members using the Scatter Plot Selection (Staid and Pieters, 2001) and the 3-Dimensional Visualizer to look at the distribution of the points within each ROI (they should cluster tightly together) and look for overlap between the classes (they should not overlap). The *n*-Dimensional Visualizer in ENVI software is an interactive tool to use for selecting the endmembers in *n*-space. Spectra can be thought of as points in an *n*-dimensional scatterplot, where *n* is the number of bands (*n* is 3 in this paper, Fig. 5a and b). The coordinates of the points in *n*-space consist of "*n*" values that are the spectral radiance or reflectance values in each band for a given pixel. The data points shown in the scatter plots for Fig. 5a and b come from the discrete selections depicted as colors in Fig. 4a and b. The distribution of these points in *n*-space can be used to estimate the number of spectral endmembers and their pure spectral signatures.

Owing to the variations in albedo, Fe and Ti mineral abundances of these basalts in this region, the 0.75 μm band reflecting albedos and two ratios (1.0/0.75 μm ratio and 0.41/0.75 μm ratio) sensitive to Fe and Ti elemental abundances are used as three axes within the 3-D Visualizer (Fig. 5a and b) to identify the number of spectral endmembers. And using average spectra can minimize some problems largely due to scattered light (Tompkins and Pieters, 1999). Groups of pixels within the 3-D Visualizer were moved to different positions as the data cloud rotates to different directions. We outlined these groups when the data cloud was rotated to an easy-to-identify position and in such situation, all the individual groups could be viewed as discrete. Each of them represents one basaltic type, with different spectral features from the others. We extracted average Clementine 5 UVVIS spectra (Fig. 5c and d) of these groups of pixels as representative spectra. These average spectra obtained and identified as reference spectra are used for subsequent supervised classification technique.

Basalt units are then reclassified using Spectral Angle Mapper (SAM) supervised classification method. The SAM is a physically-based spectral classification that uses an *n*-dimensional angle to match pixels to reference spectra. In other words, the SAM is an automated method for comparing image spectra to individual

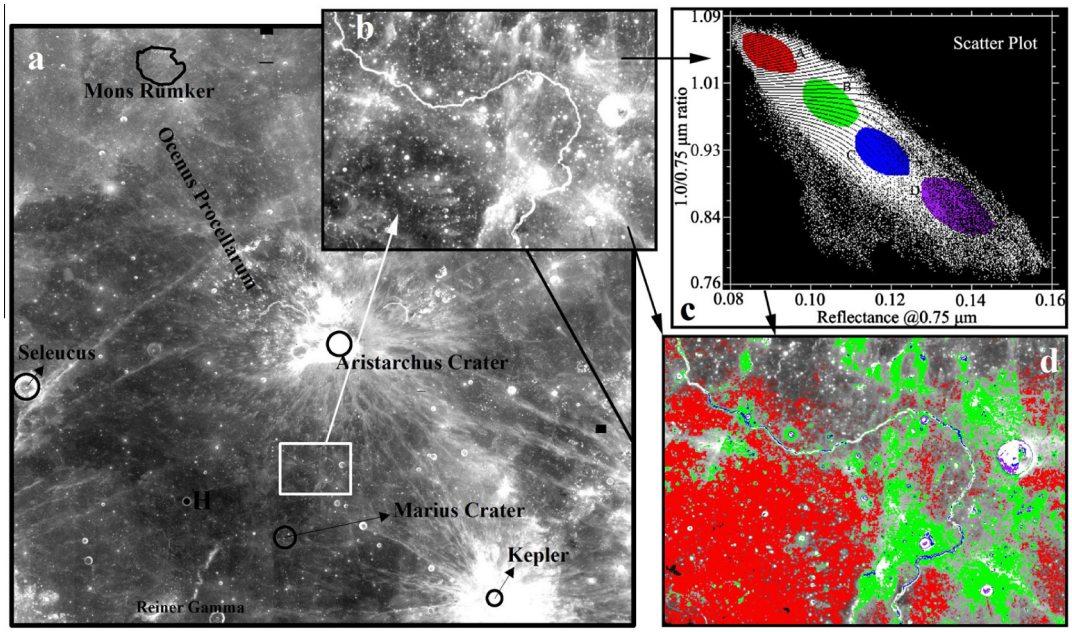


Fig. 3. ROIs of basalts selected from the upper left corner of scatterplot (0.75 μm reflectance versus 1.0/0.75 μm ratio). (a) Clementine 0.75 μm reflectance image showing the location of our mare study region. (b) An 260.4 km × 187.2 km area displayed to identify different degree of mature/immature mare soils. (c) Mafic absorption (1.0/0.75 μm ratio) versus albedo (0.75 μm reflectance) scatterplot of the region in figure b. From the plot, A (red pixels) represents the dark basalt soils, B (green pixels) indicates the ejecta and ray material of craters, C (blue pixels) shows the inner wall and rim material of craters and rilles, and D (purple pixels) represents the immature materials of craters. (d) The color map of different mare soils outlined in the scatterplot of figure c. This suggests that ROIs of basalts can be selected in the upper left corner of the 0.75 μm reflectance versus 1.0/0.75 μm ratio scatterplot. The immature materials correspond to the lower right limit of pixels cloud (D) illustrated in the scatterplot figure c. (For interpretation of the references to color in this figure legend, the reader is referred to the web version of this article.)

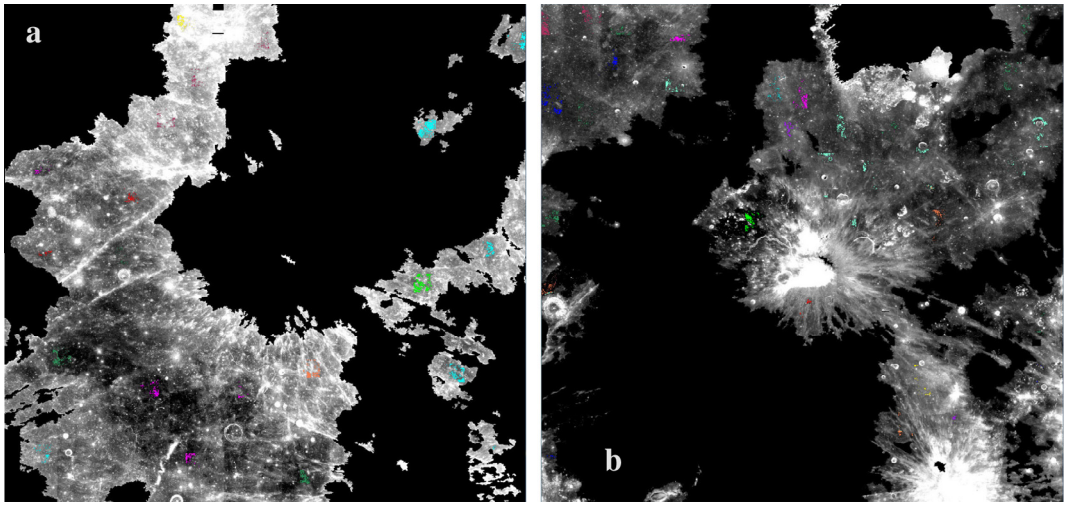


Fig. 4. Clementine 0.75 μm image showing locations of ROIs (colored pixels) selected according to the steps described in Section 3.1. (a) Pixels of ROIs selected in high-Ti region. (b) Pixels of ROIs selected in low-Ti region. TiO_2 and FeO abundance map (Lucey et al., 1996, 1998) and pixel distribution in 0.75 μm reflectance versus 1.0/0.75 μm ratio scatterplot provide help in determining these ROIs to avoid influence caused by immature materials and highland mixing. (For interpretation of the references to color in this figure legend, the reader is referred to the web version of this article.)

reference spectra selected (Kruse et al., 1993) directly from the image (extracted reference spectra as described above in this section). The algorithm determines the similarity between two spectra by calculating the angle between the spectra, treating them as vectors in a space with dimensionality equal to the number of bands. This technique, when used on calibrated reflectance data, is relatively insensitive to illumination and albedo effects (e.g., Shafri et al., 2007). SAM compares the angle between the endmember spectrum vector and each pixel vector in *n*-dimensional space. Smaller angles represent closer matches to the reference spectrum. Pixels further away than the specified maximum angle threshold (0.05 in this study) in radians are not classified. The more detailed description about SAM can be found in previous geological mapping research publications (e.g., Kruse et al., 1993; Crosta et al., 1998; Girouard et al., 2004). Basalts sub-classes are defined from the SAM supervised classification result map. The steps above used the ENVI software for data visualization and processing.

3.3. Definition of basalt units

The prerequisite to establish our criteria to define basaltic units is that a mare is the upper bound of a stack of three-dimensional

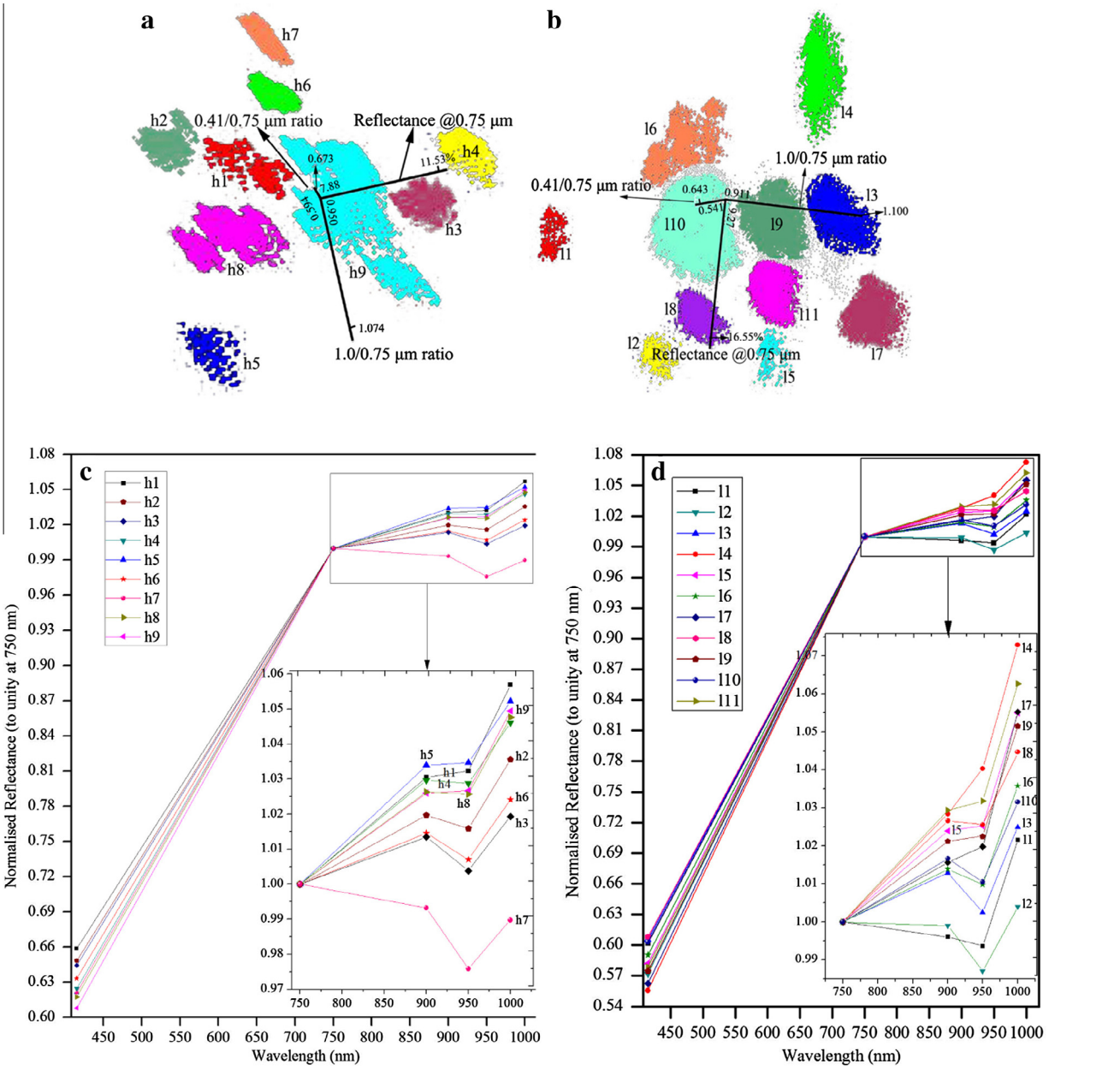


Fig. 5. (a) 3-Dimensional Visualizer of nine groups of pixels for high-Ti ROIs in Fig. 4a, H-represents high-Ti basalts. (b) 3-Dimensional Visualizer of eleven groups of pixels for low-Ti ROIs in Fig. 4b, L-represents low-Ti basalts. (c) Average spectral curves of Clementine 5 wavelength (normalized to the 750 nm reflectance) of high-Ti basalts' ROIs, corresponding to the nine pixel groups in figure a. (d) Average spectral curves of Clementine 5 wavelength (normalized to the 750 nm reflectance) of low-Ti basalts' ROIs, corresponding to the eleven pixel groups in figure b.

material layers, not merely a surface with a certain color or smoothness. The uppermost surface is a mixture of the underlying and adjacent materials, and characterizing them can constrain their distribution and probe their formation and source origin. However, it is difficult to carry out unmixing work of lunar mare soils owing to the complex mixing aspects of the impact cratering processes. The Clementine ratio composites are sensitive to spectral variations resulting from local mixing of mare with nonmare materials and variations in optical maturity (Staid et al., 2011). We assume that one spectral type indicates a whole or a portion of a flow unit composed of one type of material and state of maturity. The possible occurrence of being proportions of mixtures of impact gardened units cannot be avoided and the maturity is also one property resulting in spectral variations on the surface of one basalt unit. Therefore, one unit may contain more than one spectral type materials in this study owing to several possibilities: a range of mare basalt compositions (e.g., mixing); lunar soils suffering varying degrees of space weathering; or both of them. The focus of our classification system is to divide surface materials into different types according to their current chemical and physical state, and present a general understanding of how they evolved to the present distribution.

A quantitative value is required in order to establish a boundary condition that dictates whether or not a basalt unit is considered spectrally distinct from its neighbour. The values in Tables 3 and 4 were obtained from the measurements which were taken from a 20 km diameter circular coverage area (Fig. 6) from each basaltic unit with the least contaminated surface. When selecting the surface area to sample, we make sure to avoid crater rays that have contaminated the surface with exotic material, and thus we think best demonstrates the unit as a spectral endmember. The light highlands are poor in FeO (<10 wt%), far lower than the mare

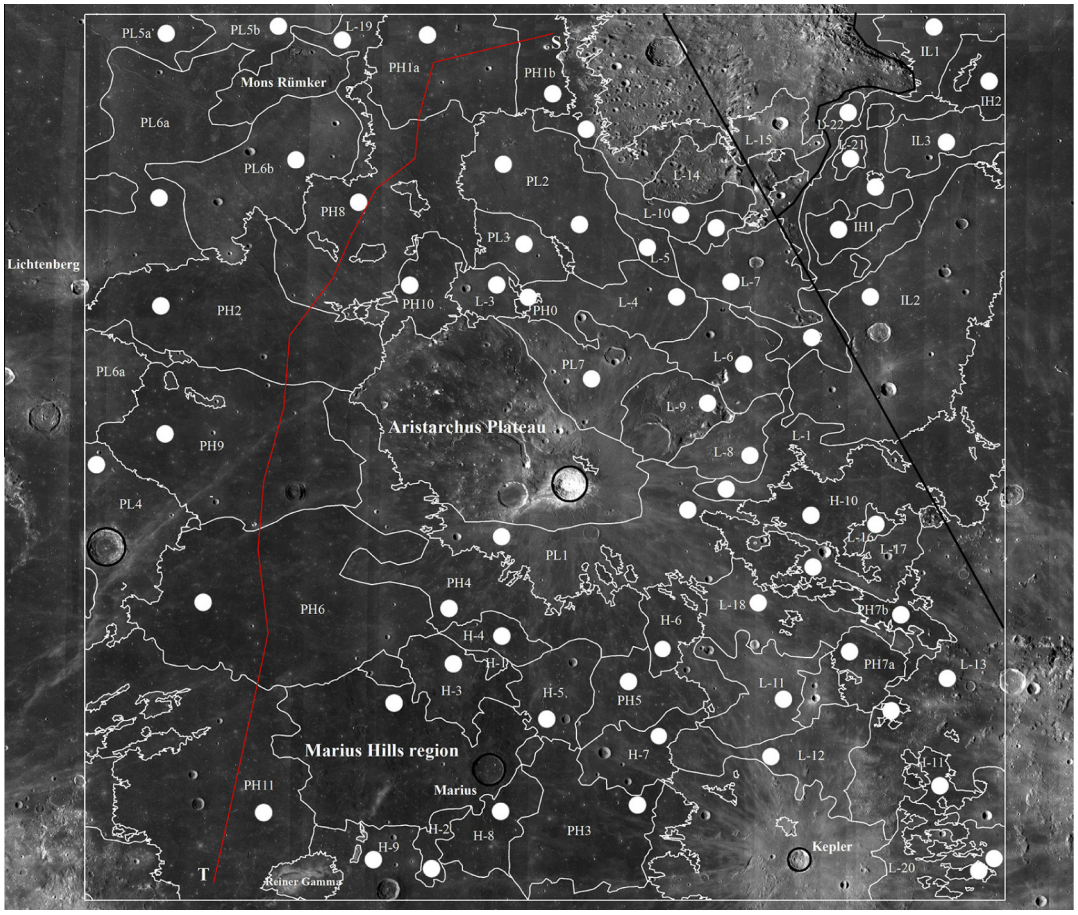


Fig. 6. The basalt units defined in this work. They are identified based on the SAM results and their boundaries are outlined by white lines. The red line ST is used to extract profiles of TiO_2 and FeO variations shown in Fig. 10. The white circle coverage area from each basaltic unit surface is used to obtain values in Tables 3 and 4. The contamination was avoided from FeO and TiO_2 abundance maps in choosing these circle coverage areas. The basemap is the LRO WAC USGS global mosaic, and simple cylindrical map projection is used. (For interpretation of the references to color in this figure legend, the reader is referred to the web version of this article.)

basalts (>16 wt% FeO) in the study region. If one surface area contaminated by exotic materials is different with it in composition, it will show compositional variations distinct from the surrounding basalt. In addition, when selecting the surface area to sample we make sure to avoid fresh impact craters large enough to have penetrated the surface basalt, exposing a different composition beneath. Impact craters excavate and uplift materials from depth as much as 1/10 of the crater diameter (Pieters et al., 1994). If the ejecta of a crater penetrating a surface mare unit contains materials of the underlying unit, the spectral parameters would be affected if these materials are included and their chemical composition is different from that of the surface unit. Those elemental maps (TiO_2 and FeO abundance) can present low TiO_2 abundance mare materials excavated from beneath the surface and low FeO highland materials emplaced in the highland impacting events. In the Clementine false color ratio map, a green, cyan, or yellow color in maria would indicate freshly exposed basalt (e.g., Heather and Dunkin, 2002; Kodama and Yamaguchi, 2003). We carefully eliminated such craters and their ejecta from the sampled area to avoid contamination by these materials.

In this paper, we assigned a simple letter/number name to each unit. The letter "P" indicates Oceanus Procellarum, and "I" expresses Mare Imbrium. The second letter stands for titanium content class type: L-for the range of 1.5–6 wt% TiO_2 and H- for the range >6 wt% TiO_2. Unlike in the geologic maps of the Moon (e.g., Hiesinger et al., 2000, 2003), lower numbers reflect younger units, and higher numbers indicate an older age. For example, "PH2" indicates that the unit is distributed in Oceanus Procellarum, with TiO_2 content >6 wt%, and is a younger age unit than PH3, but older than PH1. Units that have no defining ages in the measurements system of Hiesinger et al. (2000, 2003) will not be added to the later statistical analysis of spectra-age relationship. These units are named by simple "H-number" and "L-number" style, and the numbers contain no age order information. In order to spectrally, compositionally and stratigraphically analyze units defined in our

Table 1
The parameters used by Pieters (1978) to characterize mare basalt types from telescopic spectral reflectance.

Values	UV/VIS ratio[a]	Albedo	1 μm band	2 μm band
High	H: high (⩾1.05) h: med.high (1.02–1.05)	B: bright (⩾9.5%) I: intermediate (8–9.5%)	S: strong G: general	P: present
Low	m: medium (0.99–1.02) L: low (⩽0.99)	D: dark (⩽8%)	W: weak	A: absent

[a] UV/VIS ratio values are 'normalized' to MS2 (a standard site in Mare Serenetatis).

Table 2
Defined basalt units in the Aristarchus quadrangle from this work and stratigraphic column for the basalts in previous researches.

Unit in this study		Pieters (1978)	Boyce and Jonnson (1978) and Whitford-Stark and Head (1980)		Hiesinger et al. (2000, 2003)		Major UVVIS spectral types[a] in this study		
		Spectra type	Member	Age (b.y.)	Unit	Age (b.y.)			
Marius Hills region		Cone and dome material					h1	h4	h2
PH0		hDSA, LBG-	Schiaparelli Basalts	2.5 ± 0.5	P59	1.21	h4	h6	
PH1	PH1a	hDSA	Roris Basalt	3.2 ± 0.2	P58	1.33	h6	h4	h3
	PH1b						h8	h6	h4
PH2		HDSA, hDSA	Schiaparelli Basalts	2.5 ± 0.5	P53	1.68/3.18	h2	h3	h1
PH3		hDSA			P52	1.73/3.72	h3	h2	h6
PH4					P51	1.85	h7	h6	h3
PH5							h6	h3	h7
PH6		HDSA			P49	2.01	h3	h2	h1
PH7	PH7a				P43	2.12	h4	h6	
	PH7b								
PH8		HDSA, hDSA			P39	2.19			
PH9		hDSA			P32	2.76	h3	h2	
PH10		HDSA, hDSA			P26	2.96/3.49			
PH11		mISP	Marius Basalt	3.3 ± 0.3	P19	3.31	h8	h9	
IH1		hDSA			I28	2.62			
IH2					I22	2.96		h4	h9
H-1		Undivided	Schiaparelli Basalts	2.5 ± 0.5				h9	
H-2		hDSA	Marius Basalt	3.3 ± 0.3					
H-3		Undivided	Schiaparelli Basalts	2.5 ± 0.5			h6	h4	
H-4					P51	1.85	h3	h7	
H-5		hDSA					h6		
H-6					P51	1.85			
H-7					P52	1.73/3.72			
H-8								h4	h2
H-9		hDSA	Flamsteed Basalt		P24	3.00/3.74			h8
H-10		hDSA, undivided	Schiaparelli Basalts					h8	h7
H-11		Cone and dome material, undivided	Kunowsky Basalt				h5	h8	h9
PL1		hDSA, undivided	Schiaparelli Basalts		P60	1.20	l1	l3	
PL2		LBG-	Hermann Formation	3.3 ± 0.3	P40	2.14/3.40	l8	l5	
PL3					P31	2.88/3.72		l10	
PL4		mISP	Lavoisier Basalts	3.5 ± 0.1	P14	3.36/3.62	l6	l8	l3
PL5	PL5a	LBG-	Dechen Basalt	3.6 ± 0.2	P10	3.44	l4		
	PL5b						l7	l2	
PL6	PL6a	mISP	Lavoisier Basalts	3.5 ± 0.1	P9	3.47	l11	l10	
	PL6b						l6	l5	l2
PL7		LBG-	Aristarchus Basalt	3.65 ± 0.05	P4	3.48/3.74	l2		
IL1					I21	3.01	l7	l4	l11
IL2		LBSP	Delisle Basalt	3.2 ± 0.2	I16	3.30	l6	l2	l1
IL3					I12	3.35	l9	l7	
L-1		hDSA	Schiaparelli Basalts	2.5 ± 0.5			l3	l1	
L-2									
L-3			Hermann Formation	3.3 ± 0.3					
L-4		LBSP						l10	
L5							l6	l8	l10
L-6					P7	3.48		l2	l5
L-7		hDSA							
L-8		LBG-	Aristarchus Basalt	3.65 ± 0.05			l2		
L-9								l7	l9
L-10		LBSP, LBG-	Hermann Formation	3.3 ± 0.3			l7	l9	
L-11							l2		
L-12							l6	l10	l3
L-13		Undivided					l11	l8	l5
L-14							l4		
L-15							l11	l5	
L-16		hDSA	Schiaparelli Basalts	2.5 ± 0.5			l6	l10	l3
L-17							l3	l8	
L-18									
L-19		mISP	Lavoisier Basalts	3.5 ± 0.1			l8	l3	
L-20		Undivided	Hermann Formation	3.3 ± 0.3			l3	l8	
L-21		LBSP					l9	l7	
L-22		LBG-					l7	l4	

[a] H indicates high-Ti basalts, L represents low-Ti basalts, and the number means the types of spatially coherent units corresponding to groups of pixels in Fig. 5a and b. They are ordered according to the size of area they occupied the unit.

work, the nomenclature of basalt types characterized by Pieters (1978, see Table 1 for definition) and distribution of the four formations defined in the study of Whitford-Stark and Head (1980) are used to compare with our results. Our units are placed into the stratigraphic column of Boyce and Jonnson (1978) and Hiesinger et al. (2000, 2003), as illustrated in Table 2.

4. Results and interpretation

4.1. Spectral and compositional analysis of basalt units

The results obtained from the preliminary analysis of the SAM classification map are presented in Fig. 6. In total, more than 70

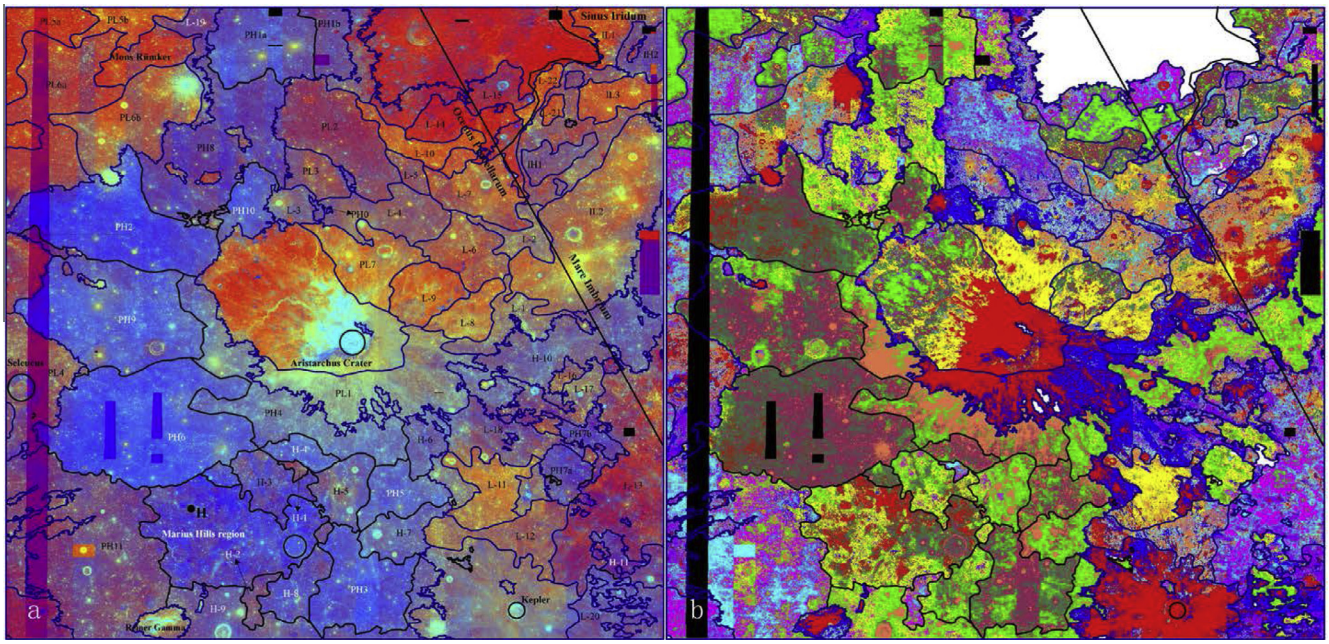


Fig. 7. Spatial distribution of spectrally defined units in the Aristarchus region. (a) The Clementine color ratio map with defined units in this study. In the map the 415/750 nm ratio is assigned to red, the 750/950 nm ratio to green, and the 750/415 nm ratio to blue. The letter H indicates a vertical hole located in a sinuous rille at the Marius Hills region and considered as a possible lava tube skylight (Haruyama et al., 2009). (b) SAM classification map of the Aristarchus region showing unit numbers and spectral types in colors (also see Fig. 5 and Table 2). White areas are non-mare materials or have been excluded from this investigation. The same color between the high-Ti and low-Ti basalts is different in compositional and spectral aspects. (For interpretation of the references to color in this figure legend, the reader is referred to the web version of this article.)

Table 3
The chemical composition and spectral parameters of high-Ti basalts derived from Clementine UVVIS data.

Unit	TiO_2 (wt%)	FeO (wt%)	750 nm (%)	415/750 nm	750/950 nm	1000/750 nm
Marius Hills region	13.6	22.7	8.09	0.660	0.971	1.056
PH1a	6.7	18.9	10.83	0.635	0.990	1.029
PH1b	6.9	20.1	10.05	0.622	0.985	1.038
PH2	12.0	21.9	8.95	0.662	0.981	1.039
PH3	11.2	22.6	8.69	0.646	0.991	1.027
PH4	8.5	22.0	9.46	0.631	1.002	1.011
PH5	9.1	21.5	9.52	0.641	0.993	1.024
PH6	13.0	22.6	8.56	0.664	0.985	1.033
PH7a	8.2	20.9	9.70	0.632	0.988	1.029
PH7b	9.2	21.3	9.25	0.634	0.980	1.043
PH8	7.2	19.7	10.04	0.626	0.977	1.040
PH9	10.2	21.7	9.49	0.653	0.998	1.021
PH10	9.8	21.1	9.74	0.653	0.994	1.020
PH11	7.3	21.8	9.28	0.612	0.993	1.031
IH1	6.9	21.1	9.57	0.612	0.985	1.040
IH2	7.4	20.8	9.51	0.620	0.981	1.047
H-1	6.3	20.9	9.89	0.610	0.995	1.025
H-2	6.7	21.3	9.70	0.613	0.997	1.025
H-3	9.3	21.4	9.40	0.639	0.986	1.034
H-4	9.6	22.2	9.44	0.644	1.009	1.006
H-5	7.7	21.7	9.66	0.625	1.003	1.014
H-6	7.8	21.2	9.80	0.629	0.999	1.016
H-7	8.7	21.9	9.38	0.632	1.000	1.015
H-8	10.7	22.6	8.61	0.637	0.986	1.033
H-9	8.9	22.0	9.04	0.626	0.985	1.038
H-10	7.9	21.5	9.54	0.624	0.995	1.022
H-11	7.1	19.0	10.06	0.625	0.967	1.061

units were identified and considered to be unique based on the spectral variations different with their surrounding basalts. Their variations in the Clementine color ratio map (Fig. 7a) and compositional variations (Tables 3 and 4) also indicate that they are distinct mare units. Most of them and their major spectral types are listed in Table 2. Some of them that are too small to be characterized by using spectral variations and elemental abundances will not be included in Table 2. The correlation between previous result maps (Hiesinger et al., 2003; Pieters and McCord, 1976; Whitford-Stark and Head, 1980) and ours is excellent, although our map reveals additional detail of subdivisions not defined in previous studies. Among our defined units (Table 2), more than 7 (i.e. H-1, H-3, H-4, H-10, PL1, L-13, and L-20) were previously classified or partially classified as "undivided" and unidentified in the work of Pieters (1978). This is most likely due to the poor spatial resolution of ground-based reflectance data compared

Table 4
The chemical composition and spectral parameters of low-Ti basalts derived from Clementine UVVIS data.

Unit	TiO_2 (wt%)	FeO (wt%)	750 nm (%)	415/750 nm	750/950 nm	1000/750 nm
PL1	4.9	18.7	11.2	0.615	0.995	1.019
PL2	4.4	17.6	10.84	0.601	0.969	1.048
PL3	3.6	17.8	11.51	0.597	0.988	1.030
PL4	5.2	20.2	10.23	0.600	0.993	1.034
PL5a	1.8	17.2	10.94	0.552	0.963	1.077
PL5b	1.3	17.4	11.93	0.553	0.991	1.037
PL6a	3.4	18.4	10.50	0.578	0.970	1.064
PL6b	3.4	18.5	10.75	0.583	0.979	1.046
PL7	1.8	18.3	10.96	0.568	1.019	0.997
IL1	2.0	18.8	11.01	0.563	0.994	1.043
IL2	4.3	19.8	10.57	0.593	0.996	1.032
IL3	2.4	18.6	10.78	0.566	0.984	1.045
L-1	4.0	17.8	11.85	0.611	0.999	1.013
L-2	4.6	19.8	10.73	0.602	1.002	1.017
L-3	5.0	18.9	11.03	0.613	0.995	1.019
L-4	4.2	18.5	11.02	0.600	0.987	1.030
L-5	4.5	18.7	10.71	0.601	0.982	1.039
L-6	4.1	19.7	10.21	0.585	0.983	1.038
L-7	3.5	18.8	11.51	0.586	0.990	1.033
L-8	2.8	19.0	12.16	0.582	1.014	1.002
L-10	1.8	18.2	11.26	0.558	0.989	1.044
L-11	2.2	18.1	11.90	0.574	1.006	1.015
L-12	3.6	18.2	11.55	0.597	0.996	1.026
L-13	4.0	16.6	10.82	0.592	0.975	1.086
L-16	5.5	20.3	10.08	0.602	0.991	1.031
L-17	5.1	18.5	11.01	0.615	0.988	1.027
L-18	4.6	17.5	11.74	0.619	0.990	1.020
L-19	4.9	17.1	11.42	0.618	0.976	1.042
L-20	4.7	15.9	12.39	0.631	0.981	1.039
L-21	2.4	18.4	10.94	0.567	0.984	1.046
L-22	1.6	17.7	11.43	0.557	0.986	1.048

with Clementine. In general, most of our units are consistent with that in the work of Hiesinger et al. (2000, 2003). However, comparing with their results, several subdivisions (i.e. PH1a and PH1b, PL6a and PL6b) of some units were distinguished in this study, while these subdivisions were not defined in the work of Hiesinger et al. (2003). These subdivisions and differences will be discussed in Section 5.

Among the lunar maria, the spectral and compositional properties, and evolution of the basalts in the Aristarchus region appear to be unique. According to the time sequence defined by Hiesinger et al. (2000, 2003, 2008), most of these western basalts erupted during the Eratosthenian period (~3.2–1.1 b.y.) and are rich in titanium (Tables 2–4), a result consistent with that obtained by telescopic spectral measurements and Apollo gamma-ray data (Pieters, 1978; Davis, 1980; Wilhelms, 1987). The resulting TiO_2 and 750 nm reflectance values extracted in Tables 3 and 4 show that dark, relatively blue mare surfaces are TiO_2-rich basalts. The FeO contents of these high-Ti basalts also reveal that these last major mare eruptions are the most iron-rich (most >20 wt% FeO). The steepness of the continuum (415/750 nm ratio) is sensitive to both composition and maturity of the soil (Pieters et al., 1994). As Tables 3 and 4 show, there is a significant difference in 415/750 nm ratio values between the high-Ti (>0.610) and the low-Ti (most <0.610) groups. This is likely dominated by the effect that ilmenite has on the spectrum. However, there is not a clear distinction between the high-Ti and low-Ti basalts for 1000/750 and 750/950 nm ratios owing to the fact that the Clementine 950 and 1000 nm wavelength are both being affected by the ferrous absorption feature.

We correlate our spectral types (Fig. 7b) with the colors of the Clementine false ratio color map (Fig. 7a). In our classification map, the h1, h2, and h3 classes of the high-Ti basalts correspond with the different state of blue color in the Clementine ratio color image. And our h4, h5, and h6 types appear purple and brown, while h8 and h9 types show pink and red colors in the Clementine ratio color map. For the low-Ti basalts, most of them appear a range of pink and red colors, except that l1 and l2 spectral types represent cyan and yellow colors from the Clementine ratio color map. This suggests that our classification system can reclassify the Clementine ratio colors into different material levels and be reproduced in detailed spectral types.

The spectra (Fig. 8) for each of our spectral types were extracted by averaging each pixel group of ROIs in Fig. 5a. Spectral variations on the surface of each basalt unit appear dominated by an absorption near 1.0 μm. The slopes of spectral curves from 950 to 1000 nm wavelength in each group (Fig. 8) are nearly the same, but have different slopes from 900 to 950 nm wavelength. The depth of the absorption at 950 nm for h3 > h2 (Fig. 8a) is consistent with the FeO abundance (Table 3) of PH3 (h3 spectral type and 22.6 wt% FeO) being greater than PH2 (h2 spectral type and 21.9 wt% FeO). From Fig. 8b, the depth of the absorption at 950 nm for h6 > h4 > h5 (Fig. 8b) is met, and is consistent with the FeO contents of H-3, H-5, H-8, H-9, and H-10 (h6 spectral type and >21 wt% FeO) being relatively greater than PH8 (h4 spectral type and 19.7 wt% FeO) and H-11 (h5 spectral type and 19.0 wt% FeO). With exposure to the space environment, lunar soils darken, redden, and exhibit reduced spectral contrast (Fischer and Pieters, 1994, 1996; Lucey et al., 2000b). The h1, h2, and h3 spectral types can be found together on a single unit (e.g., PH2, PH6, and PH9). This is also the case for the h4, h5, and h6 spectral types (e.g., PH1a and PH8) and h8 and h9 (PH1b and PH11). This all suggest that spectral variations on the surfaces of each basalt unit may be mainly dominated by compositional variations, though the space weathering effects reduce spectral contrast.

The same as the analysis of the high-Ti basalts, the spectra (extracted by averaging each pixel group of ROIs in Fig. 5b) of low-Ti basalts also suggested that our spectral diversity were caused by compositional variations, though the influence of space weathering is complex. The spectra of l3, l8, and l10 (Fig. 9a) exhibit strong ferrous iron absorptions with band minimas at 950 nm. For l1,

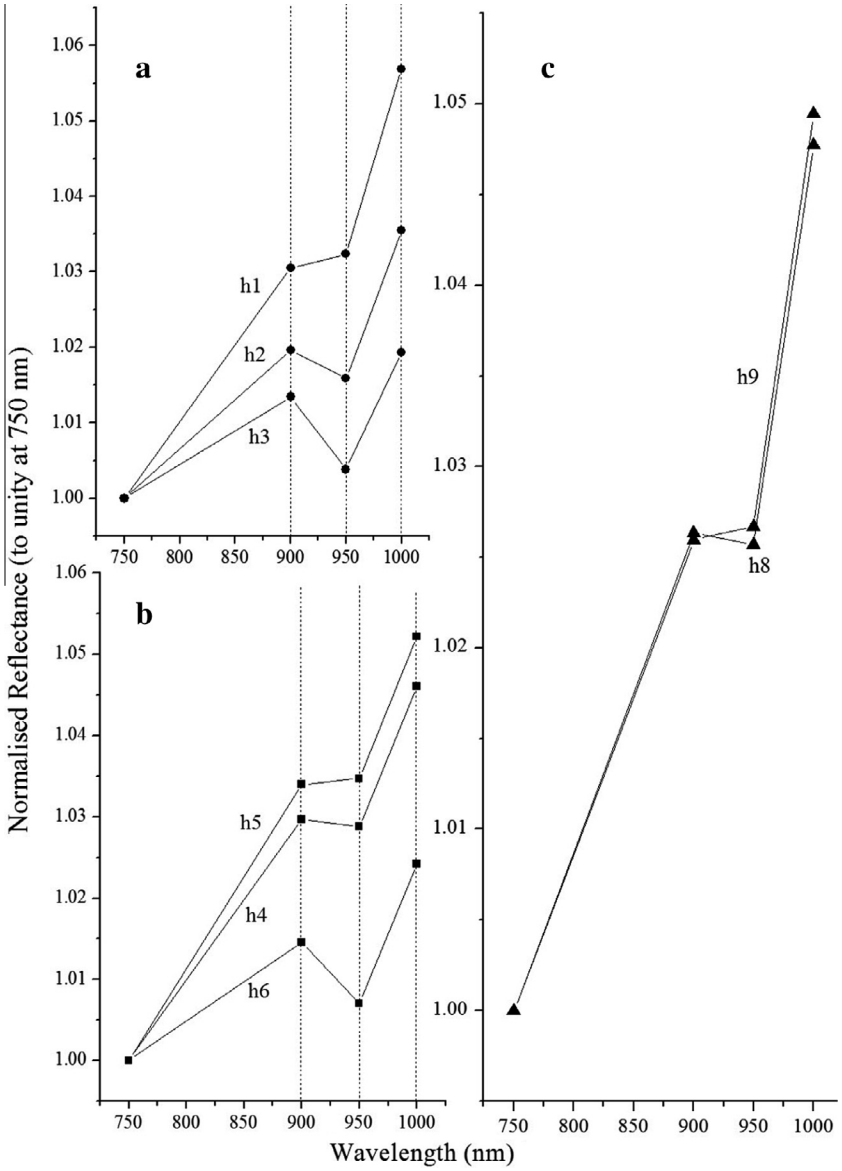


Fig. 8. The average spectra of eight high-Ti basalt types (obtained by averaging all ROIs selected in Fig. 5a. (a) Four-color Clementine spectra of h1-h3 types and (b) four-color Clementine spectra of h4-h6 classes. (c) Four-color Clementine spectra of h8 and h9 types. The slopes from wavelength 900 to 1000 nm reflect iron-bearing absorption depth. Compositional mixing due to lateral transport from impact processes, and space weathering effect complex these distinct changes. (For interpretation of the references to color in this figure legend, the reader is referred to the web version of this article.)

l2, l4, l6, and l7 spectral classes, they have different spectral shapes and iron-bearing absorption depths with each other. However, l5, l9, and l11 have a similar absorption shape with parallel normalized spectra from 900 to 1000 nm (Fig. 9b). Nevertheless, spectral types with different shapes and depths of the iron absorption occur together on the surface of one independent unit. For example, l5, l9, and l11 spectral types, which have similar shapes and depths of the iron absorption (Fig. 9b), never occurred on the same unit. This again confirms that compositional variations lead to the spectral variations on one homogeneous unit which should have one type spectrum. Those spectral variations with a range of iron-bearing absorption depth will also be a useful clue for us to investigate physical and chemical transformation of mare soils, which have undergone a long period of exposure time in the chilly space environment.

According to the spectrum-color relationship interpreted above, our spectral types are likely to be assigned to having petrological significance. In our classification scheme, blue units (Clementine ratio color, Fig. 7a) with h1, h2, and h3 spectral types appear mature high-Ti mare basalts, while red units with l2, l4, l8, and l11 spectral types appear mature low-Ti mare basalts. The green, cyan and yellow mare soils with h7 and l3 spectral types indicate freshly exposed basalt. The h1, h2, h3 type mare soils (PH2, PH6, and PH9, Fig. 7) have similar trends for TiO_2 and FeO contents (Fig. 10) along the red line ST in Fig. 6. This is also the case for the h4 and h6 spectral type mare soils on the surfaces of PH1a and PH8 units. The units PH1b and PH11 have no significant difference in TiO_2 variations with the unit PH1a and PH8, but have an obvious higher FeO content than PH1a and PH8 (Fig. 10). This indicates that the basalts with h8 and h9 types are distinct basalts with a higher FeO content than basalts with h4 and h6 types, while the similar TiO_2 content variations are observed for these basalts with h4, h6, h8 and h9 spectral types. We infer this to mean that these basalts defined in our classification system can be interpreted petrologically from their spectral variations.

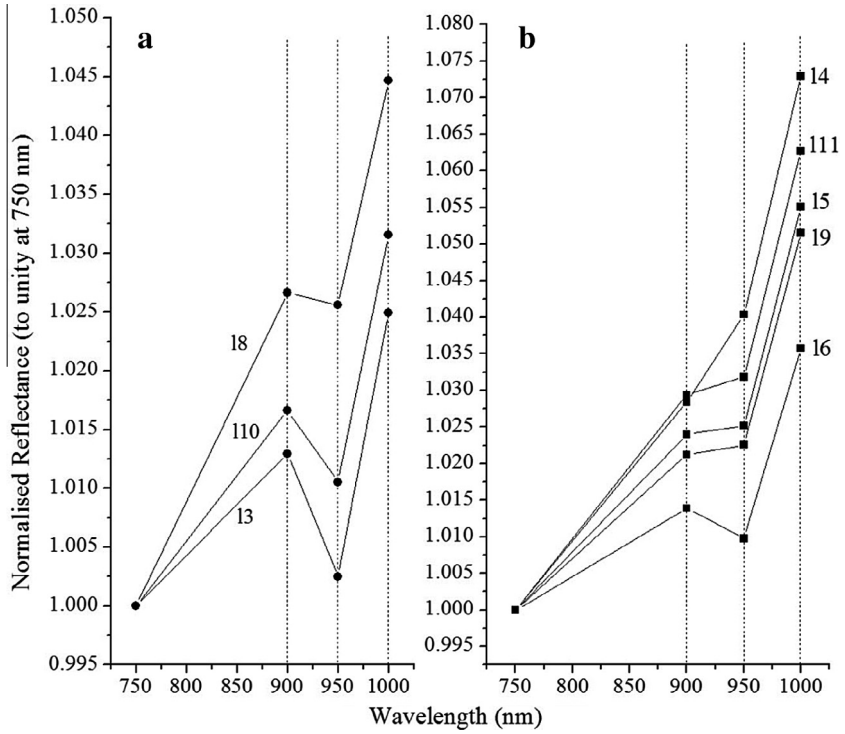


Fig. 9. The average spectra of eight low-Ti basalt types (obtained by averaging all ROIs selected in Fig. 5b). (a) Four-color Clementine spectra of l3, l8, and l10 types and (b) four-color Clementine spectra of l4, l5, l6, l9, and l11 classes.

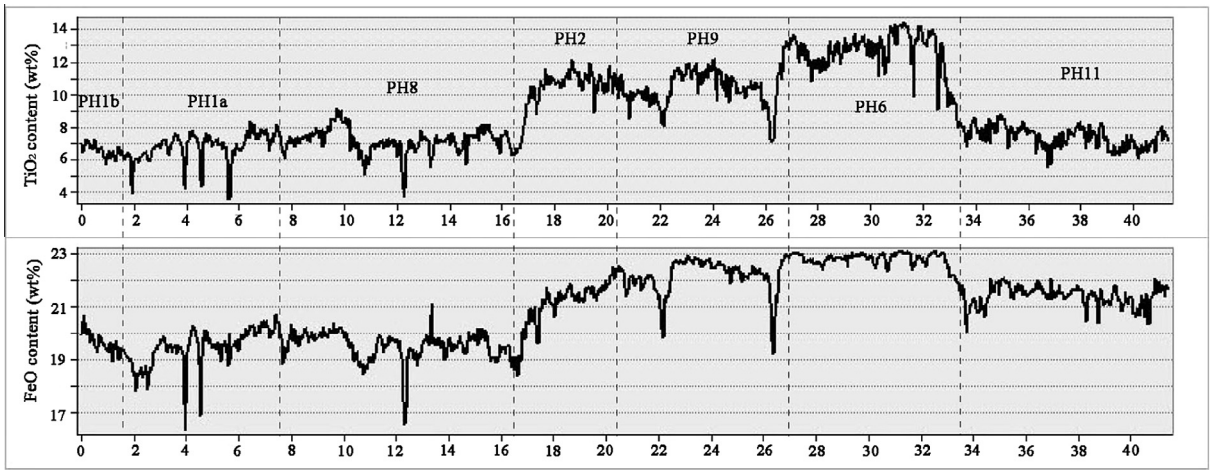


Fig. 10. Profiles of TiO_2 and FeO contents along the line ST in Fig. 6. Basalts PH2, PH6, and PH9 (h1, h2, and h3 spectral types) show the similar TiO_2 and FeO change trend. This is also the case for PH1a and PH8. However, PH1b and PH11 represent different situation.

The approach to classify basaltic units used in this paper can also be validated by detecting sub-units from their chemical analysis of TiO_2 and FeO abundance variations. Petrologic analyses of lunar samples suggest that high-titanium lunar basalts show a trend in which TiO_2 content decreases with increasing fractionation of Fe-Ti oxide minerals from the melt (Lofgren et al., 1981). Thus, an important implication of this observation is that fractionation can produce significant Ti gradients along flow lines if high-titanium lavas flow long distance. The Clementine 0.41/0.75 μm UV/VIS ratio (sensitive to Ti content) was successfully used to estimate spectral parameter trends along the Imbrium flows in the study of Staid and Pieters (2001). The similar appearance was also observed from our detecting that TiO_2 and FeO contents of units PH1a and PH1b (geologic setting see in Fig. 11) would be expected to decrease (Fig. 12a–d) along the flow lines BA and DC (from south to north, Fig. 11) referring to the flow direction (Fig. 13) defined in the study of Whitford-Stark and Head (1980). Meanwhile, we extract TiO_2 and FeO content profiles along the line EF plotted in Fig. 11 and check their change trends. The line EF walks through the surfaces of both PH1a and PH1b, and the letter G indicates the boundary between them. From the west E to east F (Fig. 12e and f), the TiO_2 content of PH1a is higher than PH1b, but lower than PH1b for FeO content. These differences between the units PH1a and PH1b cannot be easily detected by simply using the Clementine color ratio image in previous studies (e.g., Hiesinger et al., 2003), but can be distinguished from spectral variations by using the approach in this paper.

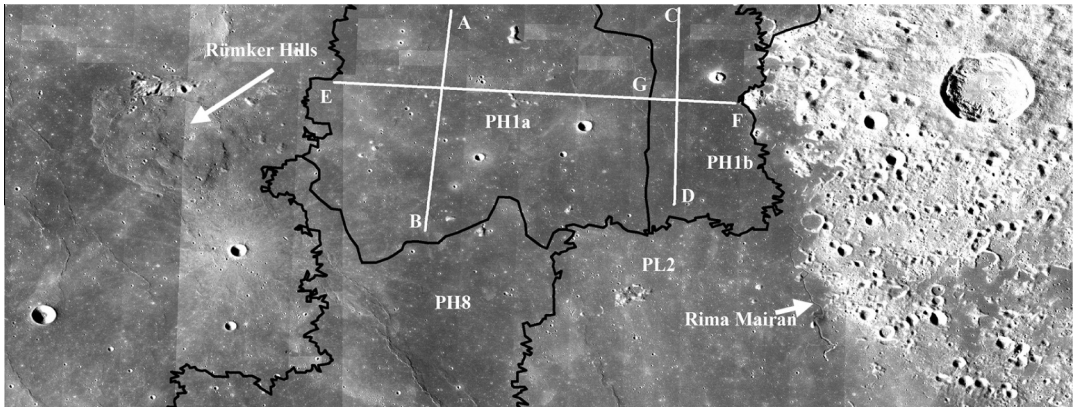


Fig. 11. LRO WAC mosaic image illustrating the context of the subunit PH1a and PH1b. The Basalt PH1b is next to the deposit surrounding the Sinus Iridium. The sinuous Rima Mairan extends into PH1b from south.

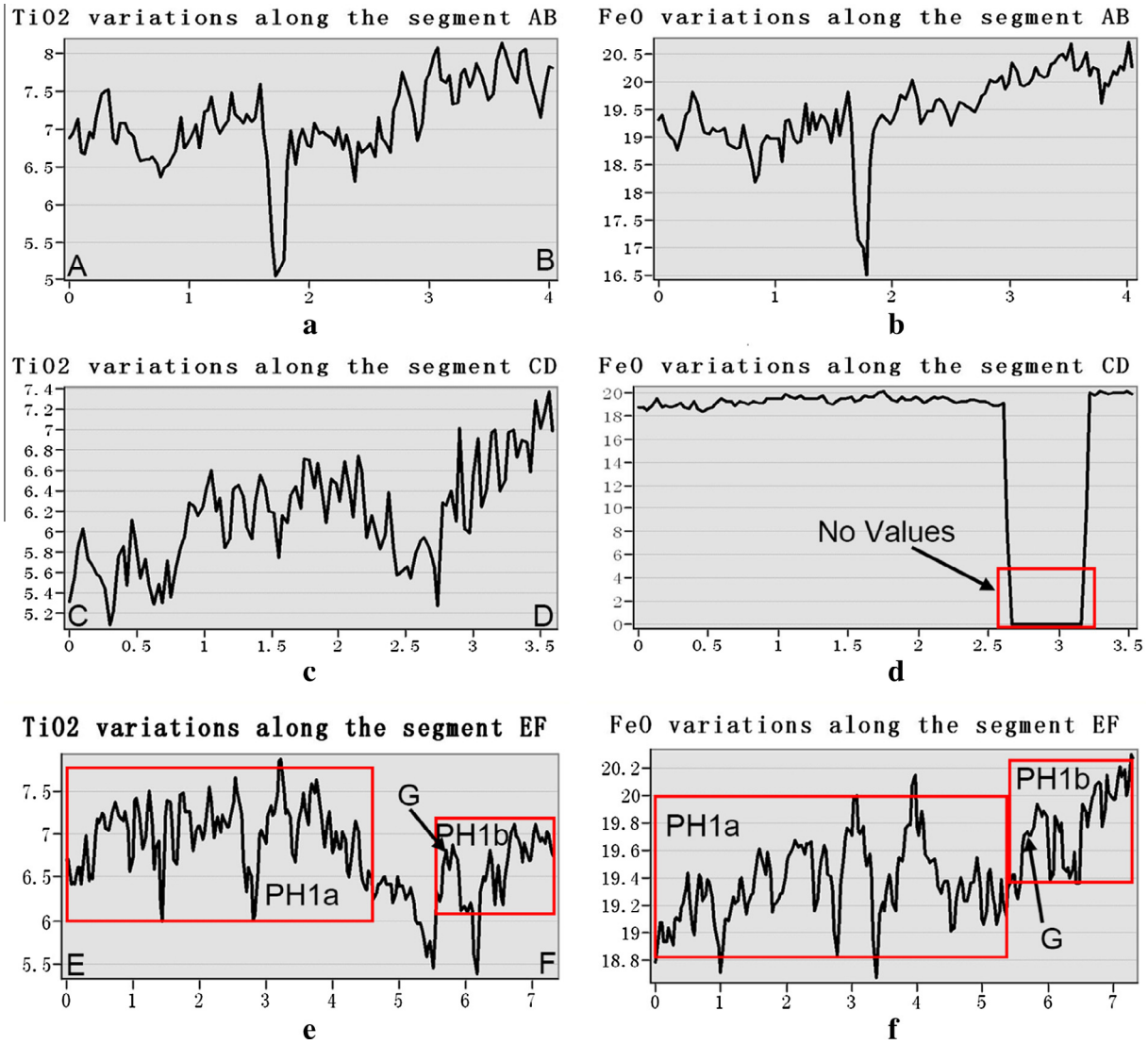


Fig. 12. Profiles of TiO_2 and FeO contents along the three lines in Fig. 11. (a) The TiO_2 and (b) FeO variations along the segment AB present their increase trends from A to B (north to south). (c) The TiO_2 and (d) FeO variations along the segment CD show their increase trends from C to D (north to south). *X*-axis indicates distance along lines (degree). (e) The TiO_2 variations along the segment EF, the average TiO_2 value of PH1a is slightly higher than PH1b. (f) The FeO variations along the segment EF, the average FeO value of PH1a is slightly lower than PH1b.

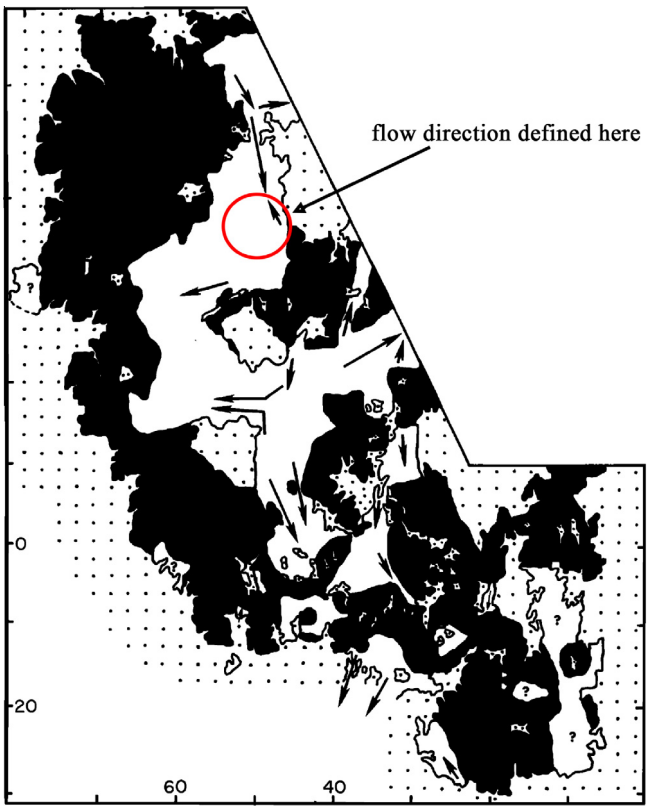


Fig. 13. Flow directions of high-Ti units defined in the work of Whitford-Stark and Head (1980). The highlands are depicted by dots and relatively older low-Ti units in black.

4.2. Implications for the stratigraphical sequence

Previous studies of lunar basalt types suggested that mare volcanism was regionally complex with no simple correlation between composition and absolute age (e.g., Pieters, 1978; Giguere et al., 2000; Hiesinger et al., 2003). This can be seen from the corresponding relationship between our spectral types and model ages measured by Hiesinger et al. (2000, 2003) using crater size–frequency distribution. A single spectral type can be observed on several basalt surfaces, which formed in different times. However, we must emphasize the fact that our classification system is based on the spectral characteristics. The two important factors that affect reflectance spectra of mare soils are the compositional variations and space weathering. Nevertheless, we believe that the spectral differences related to these two factors referred above can be detected, though they complicate the interpretation of mare basalt stratigraphy.

A potential and simple relationship between the stratigraphical sequence and the Clementine colors (related to our spectral variations) can be revealed by statistical analysis of 24 units which are consistent with ones defined by Hiesinger et al. (2000, 2003). According to the age order (from young to old) of these basalts, our spectral types together with the Clementine colors are plotted in Fig. 14. Among these 24 basalts, PL1 and PH4 appear yellow/cyan in the Clementine ratio color map (Fig. 7a). Mare basalts PH0, PH1, PH2, PH3, PH5, PH6, PH7, PH9, and PH10 appear blue, and PL2, PH8, IH1, PL3, and IH2 appear brown/purple while IL1, IL2, PH11, IL3, PL4, PL5, PL6, and PL7 appear pink/red. From Fig. 14, we can infer that the pink/red color basalts are the oldest mare units, while yellow/cyan units are the youngest. The basalts that appear blue and brown/purple colors formed between both referred above. But, most blue color units are relatively younger than brown/purple units, except for the blue units PH9 and PH10 which are older than some brown/purple ones. From our analysis, the units with h7 spectral type materials are the youngest ones among those high-Ti basalts, and the units with h8 and h9 types are the oldest. The h1, h2, and h3 spectral materials mainly occur on the units that appear blue (Fig. 14) in the Clementine false ratio color map. However, most blue units are younger than brown/purple ones in the Clementine false ratio color map except that the unit PH9 and PH10 are older than some brown/purple basalts. The unit PH10 is classified into P26 (the purple/brown color in the whole) unit in the work of Hiesinger et al. (2003). For the low-Ti basalts, the units with l1 and l3 spectral types are younger than other low TiO_2 basalts, which would appear as a range of red/pink colors in the Clementine false ratio color image.

Our statistical analysis between the surface age and TiO_2 concentrations also confirmed that TiO_2 concentrations appear to vary independently with time, and generally eruptions of TiO_2-rich and TiO_2-poor basalts have occurred contemporaneously (e.g., Hiesinger and Head, 2006). The eruption sequence of the 24 high-Ti and low-Ti basalts is illustrated in a plot (Fig. 15) of TiO_2 abundance (Lucey et al., 2000a) versus model ages from Hiesinger et al. (2003). From the plot, we can see that the eruption of low-Ti basalts in this region mainly occurred from 3.7 b.y. to 3.2 b.y. (Imbrian in age). Following the intensive eruptions of low-Ti basalts, eruptions of high-Ti basalts were episodic and lasted from 3.6 b.y. to 1.2 b.y. Generally, most low-Ti basalt eruptions in the study region occurred 3.0 b.y. ago, while high-Ti flows have been dated from >3.0 b.y. to as young as 1.20 b.y. The highest titanium (>12 wt% TiO_2) basalt (PH6, corresponds to the unit P49 in Hiesinger et al. (2003)) formed at the age of 2.01 b.y.

The highest titanium basalt units including the Marius Hill region, PH2, PH3, and PH6 (more than 10 wt% TiO_2) are not the youngest basalts. They belong to the Schiaparelli Basalts, which is about 2.5 ± 0.5 b.y. old, the youngest basalt member of the Sharp Formation defined by Whitford-Stark and Head (1980). Hiesinger et al. (2003) mapped the unit PH6 as the P49 unit in their work, of which the model age is 2.01 b.y. The major spectral types of the units PH2, PH3, and PH6 are h1, h2 and h3 types (Fig. 14), and are the highest TiO_2 content basalts (Fig. 15 and Table 3). However, the basalts PH1a and PH1b are defined as the unit P58 and the model age is 1.33 b.y. old in the work of Hiesinger et al. (2003). They are the youngest units among the high-Ti basalts, while the unit PL1 of low-Ti basalt is the youngest basalt in the study region. The TiO_2 contents (Table 3) of PH1a and PH1b are 6.7 wt% and 6.9 wt% respectively, but are far less than the >10 wt% TiO_2 of the Marius Hill region, PH2, PH3, and PH6 units. This suggests that the last active basalts in this region are the moderate-Ti basalts rather than the highest titanium basalts. This conclusion was also reached by Pieters et al. (1980) studying the late high-titanium basalts in the Flamsteed region. The low-Ti units L-1, L-2, L-16, L-17, and L-18 are not defined by Hiesinger et al. (2003), but mapped as Schiaparelli Basalts with an age of 2.5 ± 0.5 b.y. in the study of Whitford-Stark and Head (1980).

5. Discussion

5.1. High-Ti basalts

The high-Ti basalts show a young age, in the range of 2.7 ± 0.7 b.y. based on crater degradation (Boyce and Jonnson, 1978), and 1.0–3.0 b.y. based on crater density (Hiesinger et al., 2003). On the basis of the statistical analysis on the Clementine false ratio colors and our spectral classes versus ages (Fig. 14 and Section 4.2), the younger basalts of the last stages formed in the west of the Aristarchus Plateau, and include the north and the east portion of the Marius Hills region. Exposures of older high-Ti

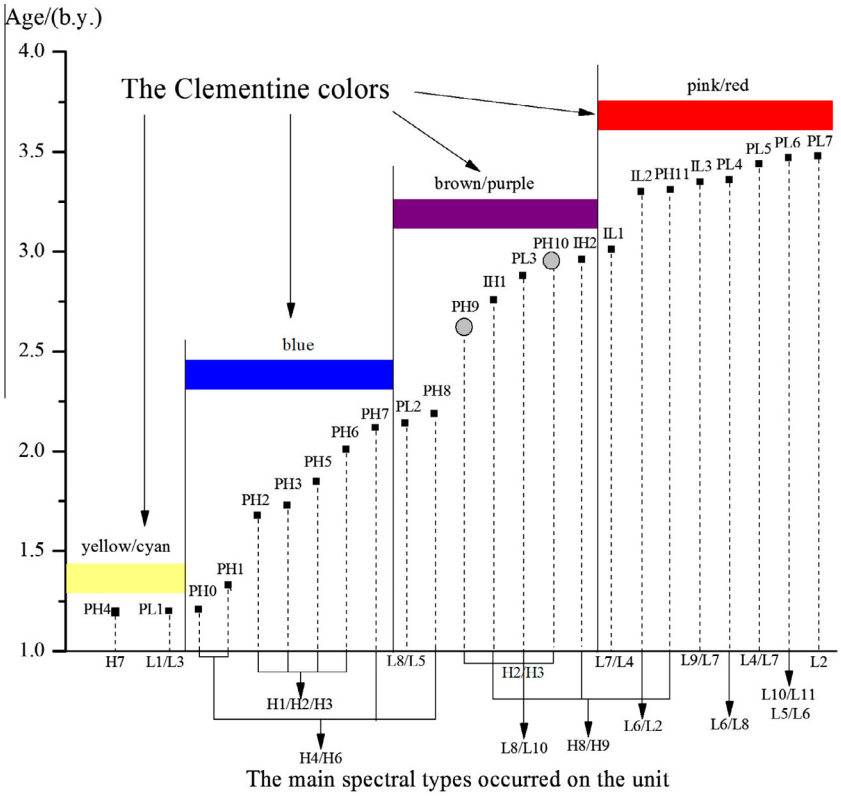


Fig. 14. The plot of Clementine ratio colors versus spectral types of basaltic units with a range of ages in this study. From left to right, these units are ordered by ages (young to old). The color bars indicate these units' colors illustrated in the Clementine false ratio color image. The units PH9 and PH10 (gray circles) appear blue in the Clementine false ratio color map but here are plotted in the brown/purple group to keep the age order of these units. From the plot, the age relationship of high-Ti basalts is that the units with h7 spectral type is the youngest basalt, and units with h8 and h9 types are the oldest, and that with h4 and h6 are between them. Among low-Ti units, the units with l1 and l3 spectral types are younger than others. (For interpretation of the references to color in this figure legend, the reader is referred to the web version of this article.)

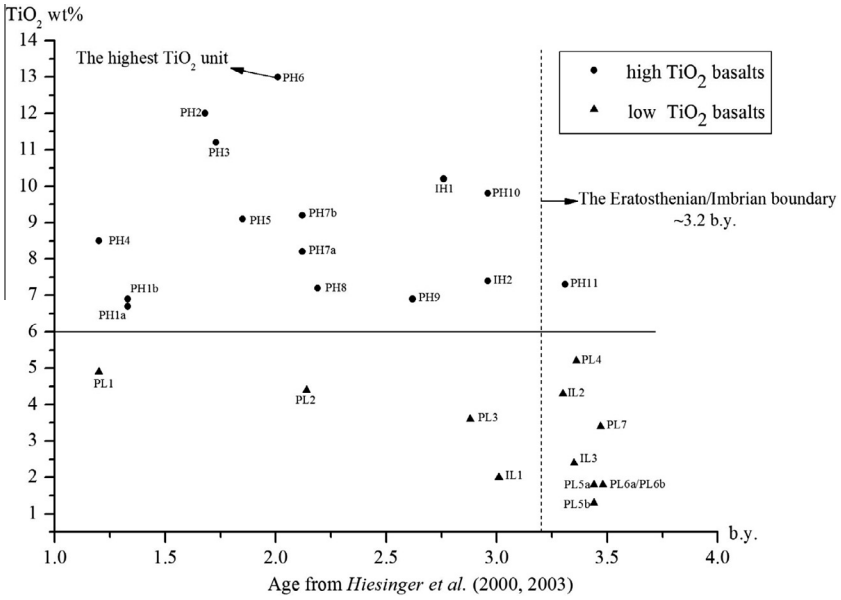


Fig. 15. The eruption time scale of basalts of different TiO_2 contents in the study area. According to the model ages defined in the work of Hiesinger et al. (2000, 2003), the intensive eruptions of low-Ti basalts cover a short time (37–32 b.y., Imbrian). But the high-Ti basalts were episodic eruptions and lasted for a long period of time (35–12 b.y.), and most formed in Eratosthenian. The most high-Ti (>12 wt% TiO_2) basalt (PH6, correspond to the unit P49 in Hiesinger et al. (2003)) formed at the age of 2.01 b.y. (For interpretation of the references to color in this figure legend, the reader is referred to the web version of this article.)

basalts are expected to be identified in west of the Marius Hills region (PH11), outer edge of the Procellarum (PH1b), northwest of Imbrium basin (IH1 and IH2), and several patches (i.e. H-1, H-2) around the Marius Hills region.

With regard to the unit PH1b, Whitford-Stark and Head (1980) classified it as Roris Basalt (Sharp Formatin), the age of which is 3.2 ± 0.2 b.y., and the hDSA spectral class defined by Pieters et al. (1980). However, using the crater size-frequency distribution

measurements method, Hiesinger et al. (2003) obtained 1.33 b.y. for the age of P58 (the nomenclature defined by Hiesinger et al. (2003)), which contains the unit PH1a and PH1b in our study. The relationship between our spectral classifications and the Clementine colors reveal that the basalt PH1b (h8 and h9 spectral types, the Clementine brown/purple color) should be the same age range as the unit PH11, IH1, and IH2, which would be closer to the age reported by Boyce and Jonnson (1978) than by Hiesinger et al. (2003). In addition, the strong 1 μm absorption within the west high-Ti mare soils may be due to the presence of abundant olivine within the emplaced basalts (Staid and Pieters, 2001). The new M^3 observations (Staid et al., 2011) of fresh craters and mare soils within the western high-Ti basalts display strong 1 μm and weak 2 μm absorptions consistent with olivine-rich basaltic compositions. Staid and Pieters (2001) also concluded that the west spectrally blue (high UV/VIS ratio) high-Ti basalts were very iron rich (>20 wt% FeO). However, the FeO contents of basalts PH1a, PH1b, PH8, and H-11 are 18–20 wt%, slightly lower than other high-Ti basalts (Fig. 16) in this region. Using Clementine UVVIS analyses and crater counts dating, the regional study of Mare Imbrium by Bugiolacchi and Guest (2008) revealed that the igneous petrogenesis of basalts in the west nearside appear to have evolved through time to more TiO_2 and FeO-rich melts.

In order to find possible evidence for making a distinction between the subunit PH1a and PH1b, we extract TiO_2 and FeO content profiles alone three lines plotted in Fig. 11 and check their change trends (analysis see in Section 4.1). From the west E to east F (Fig. 12e and f), the TiO_2 content of PH1a is higher than PH1b, but lower than PH1b for FeO content. In addition, TiO_2 content range along the line AB (6.5–8 wt% TiO_2, Fig. 12a) in PH1a is narrower than that alone CD (5.2–7.4 wt% TiO_2, Fig. 12c) in PH1b. However, FeO profiles (Fig. 12b and d) indicate that the FeO content change for both PH1a and PH1b is nearly similar. We infer this to indicate that formations of the basalt H1a and H1b, which are of slightly lower FeO content than other more TiO_2 and FeO-rich units (e.g., PH2, PH6, and PH9), are not likely to happen in the same volcanic flooding event.

Basalts around the Marius Hills appear to be predominantly Eratosthenian in age. These basalts vary from high-Ti mare basalts (H-3, H-4, H-8, and H-9; >8.9 wt% TiO_2) to relatively low titanium mare (H-1, 6.3 wt% TiO_2; H-5, 7.7 wt% TiO_2). However, all these basalts have a high FeO abundance (>20 wt%, Table 3). The basalts H-1, H-3, and H-4 were classified as "undivided" by Pieters (1978). Hiesinger et al. (2003) classified H-1 and H-3 in the Marius Hills region as a whole unit and had not defined their ages. From the SAM result map (Fig. 7b), the surfaces of the basalts H-3 and H-8 are mainly covered with materials of h6 and h4 spectral type, which correspond with the blue or brown/purple colors in the Clementine false color map. Previous geological mapping (Wilhelms and McCauley, 1971) classified H-8 as Em (Eratosthenian mare material), and H-3 as Emp (Eratosthenian mare plateau material). The stratigraphical sequence analysis (see Section 4.2) of spectra-color-age for basalt H-4 (h3), H-5 (h6), and H-9 (h6) also suggest their formation to be Eratosthenian in age.

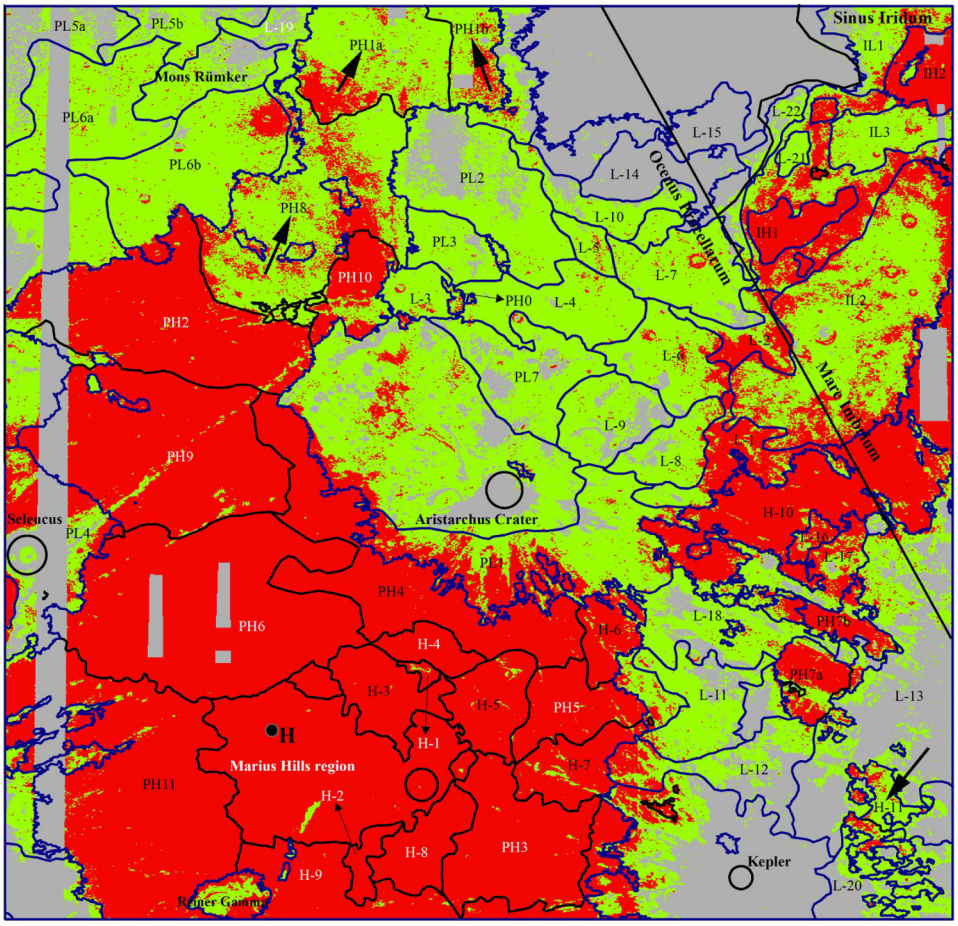


Fig. 16. FeO abundance map of the study area, constructed using algorithm of Lucey et al. (2000a). Red color represent ⩾20 wt% FeO mare materials. Green color indicate mare soils of which FeO content is between 18 and 20 wt%, and grey color shows <18 wt% mare soils and non-mare terrains. FeO contents of the most high-Ti basalts are >20 wt%, except that PH1a, PH1b, PH8, and H-11 units (marked by thick black arrows) show 18–20 wt% FeO mare soils. (For interpretation of the references to color in this figure legend, the reader is referred to the web version of this article.)

In previous work, the original surface area of the Hermann Formation includes part of the area now buried by the Sharp Formation (Whitford-Stark and Head, 1980). The Marius Basalt PH11 emplaced in southwestern Oceanus Procellarum belongs to the Hermann Formation to the west of the Marius Hills region. A major source of the basalt PH11 appears to be the Marius Hills volcanic complex, and the activity continued on the plateau after deposition of the presently exposed surface basalts of the Hermann Formation (Whitford-Stark and Head, 1980). Pieters (1978) classified the Marius Hills region, which appears to be mixing between mature low-Ti and mature high-Ti basalt from the Clementine false ratio color map, as cone and dome material. In our study, the major spectral types (h8 and h9) of H-1 and H-2 are the same as the unit PH11, as well as the units IH1 and IH2. The TiO_2 content of H-1 is 6.3 wt%, and 6.7 wt% for H-2, lower than PH11 (7.3 wt% TiO_2, Table 3). The Lunar Reconnaissance Orbiter's Wide Angle Camera mosaic (Chin et al., 2007) shows lava intrusions/extrusions occurred along the mare ridges distributed within or near the unit H-1 (Fig. 17a) and H-2 (Fig. 17b). A series of flow fronts preserved in these regions are clearly exhibited. Therefore, two possibilities for the explanation of spectrally distinct H-1 and H-2 basalts are thus suggested: (1) relatively lower TiO_2 content because of underlying low-Ti lava extrusions, and (2) H-1 and H-2 are perhaps the remnants of the Hermann Formation, which are now partly buried by later younger high-Ti basalts (Sharp Formation) coming from Marius Hills. This occurrence of the Hermann Formation at the mare ridge crests, which remained unflooded by the Sharp Formation, was also observed by Pieters et al. (1980).

5.2. Low-Ti basalts

The low-Ti basalts are depicted as the Hermann Formation of three subdivisions in Oceanus Procellarum by Whitford-Stark and Head (1980), and some part of this Formation is overlapped by the high-Ti basalts. As for the TiO_2 contents, most low-Ti units are stratigraphically older than other Ti-richer mare units (Fig. 15). In our study, a total of 11 spectral types (Fig. 5d) are identified, of which l1 type represents the youngest materials with bright-rayed impact craters (Fig. 7b). Based on our analysis in the Section 4.2, the units with l1 and l3 spectral type materials (PL1, L-1, L-2, L-3), which appear cyan/yellow in the Clementine ratio color image (Fig. 7a), are younger than ones with l4, l5, l6 and l7 spectral materials (i.e. PL4, PL5a, PL-5b, and L-10).

The attention again was focused on the PL1 basalt from the analysis of spectral variations. The spectral types of the lower age (1.20 b.y.) basalt PL1 are the l1 and l3, as well as the basalt L-1 and L-2 (Fig. 7b). The unit PL1, which is one part of the Sharp Formation in the work of Whitford-Stark and Head (1980) and lies to the south of the Aristarchus Plateau (Fig. 18), has been heavily blanketed by ejecta from the Copernican-aged crater Aristarchus (Wilhelms and McCauley, 1971). This complicates dating of the mare surface by crater density techniques and Aristarchus ejecta masks the spectral characteristics of the underlying flows (Whitford-Stark and Head, 1980). In the work of Hiesinger et al. (2003), 1.2 b.y. is obtained for the unit PL1, making it the youngest basalt unit in this region. The west portion of the unit PL1 is almost totally covered by the younger l1 spectral materials, and l3 spectral type materials cover the eastern portion of PL1 (Fig. 18b). The presence of a remnant heavily degraded ~110 km diameter unnamed pre-Imbrian age crater (South AP crater in Fig. 18a) that lies just to the south of the Aristarchus Plateau was revealed by Mustard et al. (2011) from Lunar Orbiter Laser Altimetry (LOLA) data (Smith et al., 2010). Post-Imbrian basin mare basalts have extensively flooded it and embayed the Aristarchus Plateau (Mustard et al., 2011). Exposure of l3 spectral type material (Fig. 18b) in the South AP crater and intensive ejecta distribution (Fig. 18c) of the crater Aristarchus suggest that l3 spectral type material is the main basalt type for the unit PL1, which is partially blanketed by ejecta from the Copernican-aged crater Aristarchus (Wilhelms and McCauley, 1971). Estimates of TiO_2 content of the l3 spectral type materials is >4 wt% and <4 wt% TiO_2 for the l1 spectral type material. The analysis above indicates that the low titanium materials excavated by bright-rayed Aristarchus crater masked the original basalts, affecting surface dating of the basalt PL1 based on the crater density approach. A future age analysis of a returned sample is important for an absolute determination of the basalt PL1.

The low-Ti basalts distributed in the northeast region of the Aristarchus Plateau contain various spectral type units, but the ages of several of these basalts were not measured in the work of Hiesinger et al. (2003). The three Formations (Sharp, Hermann, and Telemann) defined by Whitford-Stark and Head (1980) were observed in this region. The basalt PL2, PL3, L-1, L-2, L-3, and L-4

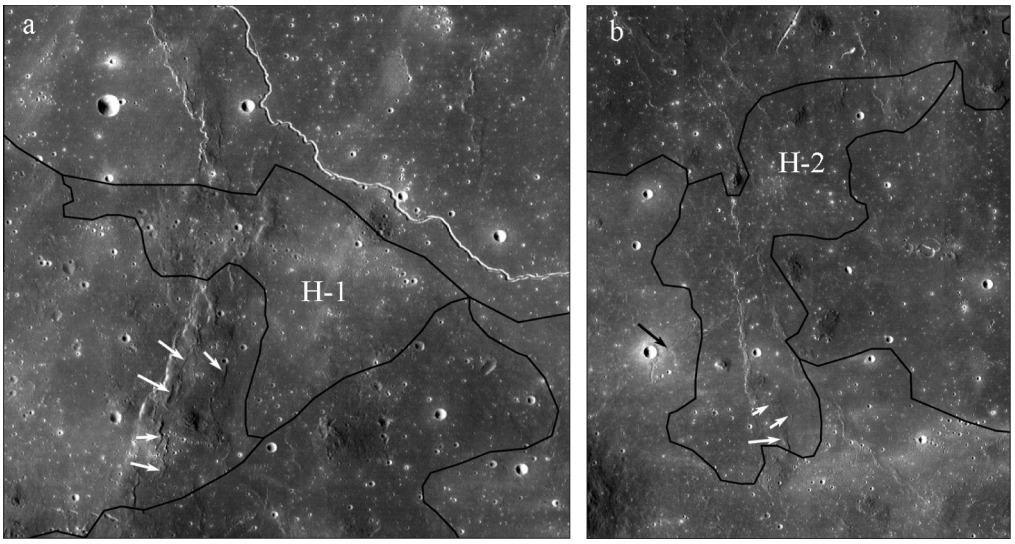


Fig. 17. The geologic context of the basalt H-1 and H-2, and LROC WAC mosaic showing wrinkle ridges occurred on the two units. (a) The geologic context of the basalt H-1. Lava extrusions and short flow fronts (white arrows) indicate stratigraphic relationship of layering basalts. (b) The geologic context of the basalt H-2. The flow fronts (white arrows) and a sinuous rille (black arrow) unravel that the intrusion/extrusion events related with mare ridges complex stratigraphic sequence in this region. (For interpretation of the references to color in this figure legend, the reader is referred to the web version of this article.)

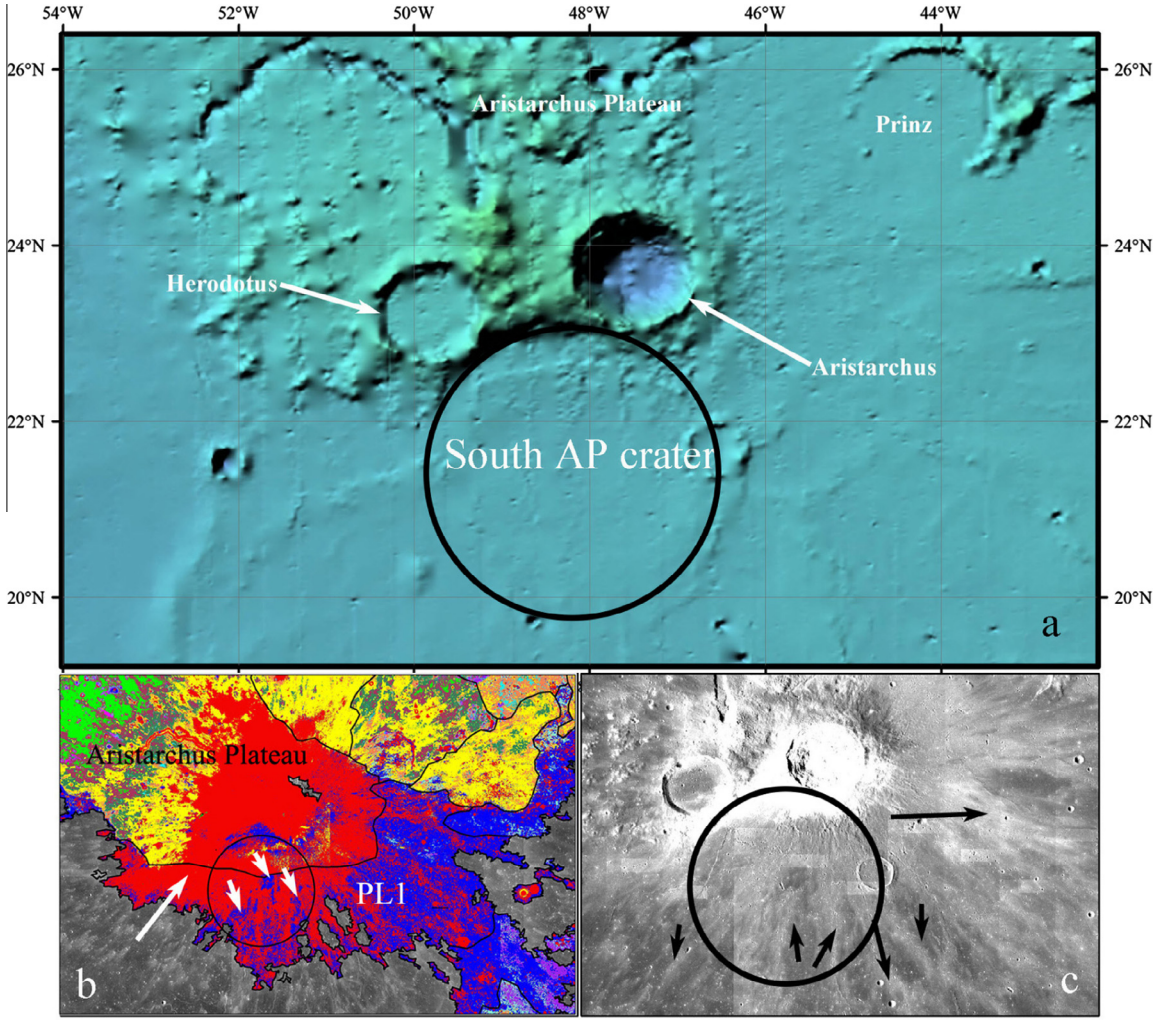


Fig. 18. (a) LOLA (Lunar Orbiter Laser Altimeter) shaded relief map for the basalt PL1 region with the South AP crater revealed by Mustard et al. (2011). (b) SAM supervised classification map to show basalt type for the unit PL1. The L1 and L3 spectral type materials are identified on the surface of the basalt PL1. L3 spectral type material is exposed (white arrow in the circle) interior of the South AP crater. (c) LRO WAC image to show the radial ejecta distributed around the bight-rayed Aristarchus crater.

are younger (l3 type) than other low-Ti basalts, which is consistent with the younger Sharp Formation in the study of Whitford-Stark and Head (1980). Wilhelms and McCauley (1971) dated L-3 as Eratosthenian in age and the surrounding basalts as Imbrian. The basalt PL7 and L-8 (l2 spectral type) are almost the oldest units in this region (northeast of the Aristarchus Plateau). This is in agreement with the Telemann Formation of these basalts defined by Whitford-Stark and Head (1980) and the P4 unit (3.48/3.74 b.y.) obtained by Hiesinger et al. (2003). Other units L-6, L-7, L-10, L-21, L-22, IL1, and IL-2 are in the middle age range in the northeast of the study area.

In the northwest of the study region, the basalts PL6a, PL6b and PL5b belong to the Hermann Formation, and are classified into the basalt member Lavoisier basalts (Table 2) by Whitford-Stark and Head (1980), but the unit PL5b is one part of the Telemann Formation. The basalts PL6a and PL6b and the basalt PL5a and PL5b are combined into the P9 (3.47 b.y.) and P10 (3.44 b.y.) units, respectively, in the work of Hiesinger et al. (2003). However, they display different spectral type materials according to our classification map (Fig. 7b). The PL5b surface is mainly covered by l7 spectral type material, but l4 for PL-5a, l11 for PL6a and l6 for PL6b. From TiO_2, and FeO content values (Table 4), PL5b (1.3 wt% TiO_2, 17.4 wt% FeO) has a similar content to PL5a (1.8 wt% TiO_2, 17.2 wt% FeO), and as well as PL6a (3.4 wt% TiO_2, 18.4 wt% FeO) to PL6b (3.4 wt TiO_2, 18.5 wt% FeO). Based on Galileo imaging observations (Greeley et al., 1993), PL6a, PL6b, PL5a are parts of the Hermann Fortation, and PL5a belongs to the Telemann Formation. In addition, according to the analysis of the Clementine false color map and our spectral variations (see Section 4.2), at least two basalt units exist on the southwest of Rümker Hills, but only one unit (P9) was defined in the work of Hiesinger et al. (2003).

6. Conclusion

We have applied the Spectral Angle Mapping (SAM) technique to Clementine UVVIS data to map spectrally distinct mare basalts in the Aristarchus region on the Moon. These multi-spectral images of high spatial resolution allow detailed mapping and improved discrimination of the mare basalts. In addition to spectral parameters that have been used in previous works, the iron and titanium contents in mare basalts were also used to characterize and classify mare units. More than 70 units were identified and considered to be distinct from their spectral variations. Generally, our analysis not only shows consistency with the results of earlier works but also newly identifies several mare basalt units. Some units newly recognized in this study are subdivisions not defined in previously studies, and it is possible that some of these subdivisions are

mixtures of adjacent impact gardened units. However, these units exhibit well-defined boundaries and spectral features distinct from their neighbors, and were mapped from high spatial resolution compositional and mineralogic information from Clementine UV-VIS data in this study.

We compared our classification system with the Clementine false color band ratio map and surface ages from the literature to unravel the spatial and temporal distributions of the regional geologic units. The relationship analysis between Clementine colors and ages indicates the relatively younger basalts which appear cyan, yellow, and blue basalts, distributed around the Aristarchus Plateau. A range of pink and red older basalts are located on the outer edge of the mare region in this study. Meanwhile, a potential relationship between composition with maturity and ages was found when correlating our spectral variations with Clementine ratio colors. In our classification scheme, blue units with h1, h2, and h3 spectral types are mature high-Ti mare basalts, while red units with l2, l4, l8, and l11 spectral types are mature low-Ti mare basalts. The green, cyan and yellow mare soils with h7 and l3 spectral types indicate freshly exposed basalt.

Our composition-age statistical analysis again confirmed that TiO_2 concentrations appear to vary independently with time, and generally eruptions of TiO_2-rich and TiO_2-poor basalts have occurred contemporaneously. The regional stratigraphic analysis of high-Ti and low-Ti basalts in the Aristarchus region indicates that intensive eruption of low-Ti mare basalts occurred during the early stages and finished in a short time, but the eruptions of high-Ti basalts were episodic and last for a long period of time. The last active basalts in this region are the moderately Ti-rich basalts rather than the highest titanium basalts.

The stratigraphy of mare units defined from our spectral analysis reveals the temporal change with their spatial distribution. The younger high-Ti basalts are concentrated around the Aristarchus Plateau and the Marius Hills region, and the relative older low-Ti basalts are located around the outer edge of the basin. The mineralogical characteristics and statistical analysis of the spectra and age relationship in the Marius Hills region indicates that early basalts may still be exposed at the surface deposit after prolonged volcanic activity in this region of the Moon. This is a result of not being blanketed by later lava flows, or lava extrusions of underlying low-Ti basalts.

Acknowledgments

This work was supported by the National Science Foundation of China (40904051), the 863 Program (2009AA122201), Science and Technology Development Fund in Macao SAR (Grant Number: 048/2012/A2) and the Hong Kong Scholar Program.

References

Belton, M.J.S. et al., 1992. Lunar impact basins and crustal heterogeneity-new western limb and far side data from Galileo. Science 255, 570–576.
Belton, M.J.S. et al., 1994. Galileo multi-spectral imaging of the north polar and eastern limb regions of the Moon. Science 264, 1112–1115.
Besse, S. et al., 2011. Compositional variability of the Marius Hills volcanic complex from the Moon Mineralogy Mapper (M^3). J. Geophys. Res. 116, E00G13.
Blewett, D.T., Lucey, P.G., Hawke, B.R., Jolliff, B.L., 1997. Clementine images of the lunar sample-return stations: Refinement of FeO and TiO_2 mapping techniques. J. Geophys. Res. 102, 16319–16325.
Boardman, J.W. et al., 2011. Measuring moonlight: An overview of the spatial properties, lunar coverage, selenolocation, and related Level 1B products of the Moon Mineralogy Mapper. J. Geophys. Res. 116, E00G14.
Boyce, J.M., Jonnson, D.A., 1978. Ages of flow units in the far eastern maria and implications for basin-filling history. Proc. Lunar Planet. Sci. Conf. 9, 3275–3283.
Bugiolacchi, R., Guest, J.E., 2008. Compositional and temporal investigation of exposed lunar basalts in the Mare Imbrium region. Icarus 197, 1–18.
Burns, R.G., 1993. Origin of electronic spectra of minerals in the visible to near-infrared region. In: Pieters, C., Englert, P. (Eds.), Remote Geochemical Analysis: Elemental and Mineralogical Composition. Cambridge Univ. Press, Cambridge, UK, pp. 3–27.
BASALTIC VOLCANISM STUDY PROJECT, 1981. Basaltic Volcanism on the Terrestrial Planets. Pergamon Press, Inc., New York, USA. 1286pp.
Cameron, W.S., 1972. Comparative analyses of observations of lunar transient phenomena. Icarus 16, 339–387.
Charette, M.P., McCord, T.B., Pieters, C., Adams, J.B., 1974. Application of remote spectral reflectance measurements to lunar geology classification and determination of titanium content of lunar soils. J. Geophys. Res. 79, 1605–1613.
Chevrel, S.D., Pinet, P.C., Daydou, Y., Le Mouélic, S., Langevin, Y., Costard, F., Erard, S., 2009. The Aristarchus Plateau on the Moon: Mineralogical and structural study from integrated Clementine UV–VIS–NIR spectral data. Icarus 199, 9–24.
Chin, G. et al., 2007. Lunar Reconnaissance Orbiter overview: The instrument suite and mission. Space Sci. Rev. 129, 391–419.
Cintala, M.J., Spudis, P.D., Hawke, B.R., 1985. Lunar bases and space activities of the 21st century. Lunar Planet. Inst. (LPI), 223–237.
Crosta, A.P., Sabine, C., Taranik, J.V., 1998. Hydrothermal alteration mapping at Bodie California, using AVIRIS hyperspectral data. Remote Sensing Environ. 65, 309–319.
Davis, P.A., 1980. Iron and titanium distribution on the Moon from orbital gamma ray spectrometry with implications for crustal evolutionary models. J. Geophys. Res. 85, 3209–3224.
Fischer, E.M., Pieters, C.M., 1994. Remote determination of exposure degree and iron concentration of lunar soils using VIS-NIR spectroscopic methods. Icarus 111, 475–488.
Fischer, E.M., Pieters, C.M., 1996. Composition and exposure age of the Apollo 16 Cayley and Descartes regions from Clementine data: Normalizing the optical effects of space weathering. J. Geophys. Res. 101, 2225–2234.
Giguere, T.A., Taylor, G.J., Hawke, B., Lucey, P.G., 2000. The titanium contents of lunar mare basalts. Meteorit. Planet. Sci. 35, 193–200.
Gillis, J.J., Jolliff, B.L., 2003. A revised algorithm for calculating TiO_2 from Clementine UVVIS data: A synthesis of rock, soil, and remotely sensed TiO_2 concentrations. J. Geophys. Res. 108 (E2), 5009.
Girouard, G., Bannari, A., Harti, A., Desrochers, A., 2004. Validated spectral angle mapper algorithm for geological mapping: Comparative study between QuickBird and Landsat-TM. In: Proceedings of the International Society for Photogrammetry and Remote Sensing, Istanbul, Turkey, pp. 12–23.
Gorenstein, P., Bjorkholm, P., 1973. Detection of radon emanation from the crater Aristarchus by the Apollo 15 alpha particle spectrometer. Science 179, 792–794.
Greeley, R. et al., 1993. Galileo imaging observations of lunar maria and related deposits. J. Geophys. Res. 98, 17183–17205.
Green, R.O. et al., 2011. The Moon Mineralogy Mapper (M3) imaging spectrometer for lunar science: Instrument description, calibration, on-orbit measurements, science data calibration and on-orbit validation. J. Geophys. Res. 116, E00G19.
Grove, T.L., Krawczynski, M.J., 2009. Lunar mare volcanism: Where did the magmas come from? Elements 5, 29–34.
Hackman, R.J., 1962. Geologic map and sections of the Kepler region of the Moon. USGS Map I-355, Scale: 1:1,000,000.
Hagerty, J.J., Lawrence, D.J., Hawke, B.R., Gaddis, L.R., 2009. Thorium abundances on the Aristarchus Plateau: Insights into the composition of the Aristarchus Pyroclastic glass deposits. J. Geophys. Res. 114, E04002.
Haruyama, J. et al., 2009. Possible lunar lava tube skylight observed by selene cameras. Geophys. Res. Lett. 36, 21206–21210.
Head, J.W., 1976. Lunar volcanism in space and time. Rev. Geophys. 14, 265–300.
Head, J.W. et al., 1993. Lunar impact basins: New data for the western limb and far side (orientale and south pole-aitken basins) from the first Galileo flyby. J. Geophys. Res. 98, 17149–17181.
Heather, D.J., Dunkin, S.K., 2002. A stratigraphic study of southern Oceanus Procellarum using Clementine multispectral data. Planet. Space Sci. 50, 1299–1309.
Heather, D.J., Dunkin, S.K., Spudis, P.D., Bussey, D.B.J., 1999. A multispectral analysis of the Flamsteed region of Oceanus Procellarum. In: Workshop on news views of the Moon II: Understanding the Moon through the integration of diverse datasets, LPI Contribution No. 980. Lunar and Planetary Institute, Houston, pp. 24–26.
Hiesinger, H., Head, J.W., 2006. New views of lunar geoscience: An introduction and overview. Rev. Mineral. Geochem. 60, 1–81.
Hiesinger, H., Jaumann, R., Neukum, G., Head III, J.W., 1996. Mare australe: New results from lunar orbiter and Clementine UV/VIS imagery. Lunar Planet. Sci. Conf. 27, 545–546.
Hiesinger, H., Jaumann, R., Neukum, G., Head III, J.W., 2000. Ages of mare basalts on the lunar nearside. J. Geophys. Res. 105, 29239–29275.
Hiesinger, H., Head III, J., Wolf, U., Jaumann, R., Neukum, G., 2003. Ages and stratigraphy of mare basalts in Oceanus Procellarum, mare nubium, mare cognitum, and mare insularum. J. Geophys. Res. 108, 5065–5091.
Hiesinger, H., Head, J.W., Wolf, U., Neukum, G., Jaumann, R., 2008. Ages of mare basalts on the lunar farside: A synthesis. Lunar Planet. Sci. Conf. 39, 1269 (abstract).
Holt, H.E., 1974. Geologic map of the purbach quadrangle of the Moon. USGS Map I-822 (LAC-95), Scale:1:1,000,000.
Johnson, T.V., Mosher, J.A., Matson, D.L., 1977a. Lunar spectral units – A northern hemispheric mosaic. Proc. Lunar Planet. Sci. Conf. 8, 1013–1028.
Johnson, T.V., Saunders, R.S., Matson, D.L., Mosher, J.A., 1977b. A TiO_2 abundance map for the northern maria. Proc. Lunar Planet. Sci. Conf. 8, 1029–1036.

Johnson, J.R., Larson, S.M., Singer, R.B., 1991. Remote sensing of potential lunar resources 1. Near-side compositional properties. J. Geophys. Res. 96, 18861–18882.
Kodama, S., Yamaguchi, Y., 2003. Lunar mare volcanism in the eastern nearside region derived from Clementine UV/VIS data. Meteorit. Planet. Sci. 38, 1461–1484.
Kodama, S., Yamaguchi, Y., 2005. Mare volcanism on the Moon inferred from Clementine UVVIS data. Lunar Planet. Sci. Conf. 36, 1641 (abstract).
Kramer, G.Y., Jolliff, B.L., Neal, C.R., 2008a. Distinguishing high-alumina mare basalts using Clementine UVVIS and Lunar Prospector GRS data: Mare Moscoviense and Mare Nectaris. J. Geophys. Res. 113, E01002.
Kramer, G.Y., Jolliff, B.L., Neal, C.R., 2008b. Searching for high alumina mare basalts using Clementine UVVIS and Lunar Prospector GRS data: Mare Fecunditatis and Mare Imbrium. Icarus 198, 7–18.
Kruse, F. et al., 1993. The spectral image processing system (sips) – Interactive visualization and analysis of imaging spectrometer data. Remote Sensing Environ. 44, 145–163.
Le Bas, M.J., 2001. Report of the working party on the classification of the lunar igneous rocks. Meteorit. Planet. Sci. 36, 1183–1188.
Lofgren, G.E. et al., 1981. Petrology and chemistry of terrestrial, lunar and meteoritic basalts. The Basaltic Volcanism Study Project. Basaltic Volcanism Terr. Planets 10, 1–437.
Longhi, J., 1992. Experimental petrology and petrogenesis of mare volcanics. Geochim. Cosmochim. Acta 56, 2235–2251.
Lucchitta, B.K., 1978. Geologic map of the north side of the Moon. USGS Map I-1062, Scale:1:5,000,000.
Lucey, P.G., Blewett, D.T., Johnson, J.L., Taylor, G.J., Hawke, B.R., 1996. Lunar titanium content from UV–VIS measurements. Lunar Planet. Sci. Conf. 27, 781–782.
Lucey, P.G., Blewett, D.T., Hawke, B.R., 1998. Mapping the FeO and TiO_2 content of the lunar surface with multispectral imagery. J. Geophys. Res. 103, 3679–3699.
Lucey, P.G., Blewett, D.T., Jolliff, B.L., 2000a. Lunar iron and titanium abundance algorithms based on final processing of Clementine ultraviolet–visible images. J. Geophys. Res. 105, 20297–20305.
Lucey, P.G., Blewett, D.T., Taylor, G.J., Hawke, B.R., 2000b. Imaging of lunar surface maturity. J. Geophys. Res. 105, 20377–20386.
McCauley, J.F., 1967. Geologic map of the Hevelius region of the Moon. USGS Map I-491 (LAC-56), Scale:1:1,000,000.
McCauley, J.F., 1973. Geologic map of the Grimaldi quadrangle of the Moon. USGS Map I-740 (LAC-74), Scale:1:1,000,000.
McCord, T.B., Johnson, T.V., 1970. Lunar Spectral Reflectivity (0.30–2.50 μm) and implications for remote mineralogical analysis. Science 169, 855–858.
McCord, T.B., Charette, M.P., Johnson, T.V., Lebofsky, L.A., Pieters, C.M., Adams, J.B., 1972a. Lunar spectral types. J. Geophys. Res. 77, 1349–1359.
McCord, T.B., Charette, M.P., Johnson, T.V., Lebofsky, L.A., Pieters, C.M., 1972b. Spectrophotometry (0.3–1.1 μm) of visited and proposed Apollo lunar landing sites. Earth Moon Planets 5, 52–89.
McCord, T.B., Pieters, C., Feierberg, M.A., 1976. Multispectral mapping of lunar-surface using ground-based telescopes. Icarus 29, 1–34.
McEwen, A.S., Robinson, M.S., 1997. Mapping of the Moon by Clementine. Adv. Space Res. 19, 1523–1533.
McEwen, A.S., Robinson, M.S., Eliason, E.M., Lucey, P.G., Duxbury, T.C., Spudis, P.D., 1994. Clementine observations of the Aristarchus region of the Moon. Science 266, 1858–1862.
Melendrez, D.E., Johnson, J.R., Larson, S.M., Singer, R.B., 1994. Remote sensing of potential lunar resources 2. High spatial resolution mapping of spectral reflectance ratios and implications for nearside mare TiO_2 content. J. Geophys. Res. 99, 5601–5619.
Moore, H.J., 1965. Geologic map of the Aristarchus region of the Moon. USGS Map I-465, Scale: 1:1,000,000.
Moore, H.J., 1967. Geologic map of the Seleucus quadrangle of the Moon. USGS Map I-527, Scale: 1:1,000,000.
Mustard, J.F., Head, J.W., 1996. Buried stratigraphic relationships along the southwestern shores of Oceanus Procellarum: Implications for early lunar volcanism. J. Geophys. Res. 101, 18913–18925.
Mustard, J.F. et al., 2011. Compositional diversity and geologic insights of the Aristarchus crater from Moon Mineralogy Mapper data. J. Geophys. Res. 116, E00G12.
Neal, C.R., Taylor, L.A., 1992. Petrogenesis of mare basalts: A record of lunar volcanism. Geochim. Cosmochim. Acta 56, 2177–2211.
Nozette, S. et al., 1994. The Clementine Mission to the Moon: Scientific overview. Science 266, 1835–1839.
PaPike, J.J., Hodges, F.N., Bence, A.E., Cameron, M., Rhodes, J.M., 1976. Mare basalts: Crystal chemistry, mineralogy, and petrology. Rev. Geophys. Space Phys. 14, 475–540.
Papike, J.J., Ryder, G., Shearer, C.K., 1998. Lunar samples. In: Papike, J.J. (Ed.), Reviews in Mineralogy. Planetary Materials. Mineralogical Society of America, Washington (1-5–5-234, Chapter 5).
Pieters, C.M., 1977. Characterization of lunar basalt types. II – Spectral classification of fresh mare craters. Proc. Lunar Planet. Sci. Conf. 8, 1037–1048.
Pieters, C.M., 1978. Mare basalt types on the front side of the Moon – A summary of spectral reflectance data. Proc. Lunar Planet. Sci. Conf. 9, 2825–2849.
Pieters, C.M., McCord, T.B., 1976. Characterization of lunar mare basalt types. I – A remote sensing study using reflection spectroscopy of surface soils. Proc. Lunar Planet. Sci. Conf. 7, 2677–2690.
Pieters, C.M., Head, J.W., Adams, J.B., McCord, T.B., Zisk, S.H., Whitford-Stark, J.L., 1980. Late high-titanium basalts of the western maria: Geology of the flamsteed region of Oceanus Procellarum. J. Geophys. Res. 85, 3913–3938.
Pieters, C.M. et al., 1993. Crustal diversity of the Moon: Compositional analyses of Galileo solid state imaging data. J. Geophys. Res. 98, 17127–17148.
Pieters, C.M., Staid, M.I., Fischer, E.M., Tompkins, S., He, G., 1994. A sharper view of impact craters from Clementine data. Science 266, 1844–1848.
Pieters, C.M., He, G., Tompkins, S., Staid, M.I., Fischer, E.M., 1995. The low-Ti basalts of Tsiolkovsky as seen by Clementine. Lunar Planet. Sci. Conf. 26, 1121–1122.
Robinson, M.S., Hawke, B.R., Lucey, P.G., Smith, G.A., 1992. Mariner 10 multispectral images of the eastern limb and farside of the Moon. J. Geophys. Res. 97, 18265–18274.
Schaber, G.G., 1969. Geologic map of the Sinus Iridum quadrangle of the Moon. USGS Map I-602, Scale: 1:1,000,000.
Scott, D.H., Eggleton, R.E., 1973. Geologic map of the Rümker quadrangle of the Moon. USGS Map I-805, Scale: 1:1,000,000.
Scott, D.H., McCauley, J.F., Mareta, N.W., 1977. Geologic map of the west side of the Moon. USGS Map I-1034, Scale 1:5,000,000.
Shafri, H.Z.M., Suhaili, A., Mansor, S., 2007. The performance of maximum likelihood, spectral angle mapper, neural network and decision tree classifiers in hyperspectral image analysis. J. Comput. Sci. 3 (6), 419–423.
Shearer, C., Papike, J., 1999. Magmatic evolution of the Moon. Am. Mineral. 84, 1469–1494.
Smith, D.E., Zuber, M.T., Jackson, G.B., Cavanaugh, J.F., et al., 2010. The Lunar Orbiter Laser Altimeter investigation on the Lunar Reconnaissance Orbiter mission. Space Sci. Rev. 150, 209–241.
Soderblom, L.A., Lebofsky, L.A., 1972. Technique for rapid determination of relative ages of lunar areas from orbital photography. J. Geophys. Res. 77, 279–296.
Staid, M.I., Besse, S., 2013. Spectral and stratigraphic mapping of lava flows in Mare Imbrium. Lunar Planet. Sci. Conf. 44, 2661 (abstract).
Staid, M.I., Pieters, C.M., 2000. Integrated spectral analysis of mare soils and craters: Applications to eastern nearside basalts. Icarus 145, 122–139.
Staid, M.I., Pieters, C.M., 2001. Mineralogy of the last lunar basalts – Results from Clementine. J. Geophys. Res. 106, 27887–27900.
Staid, M.I. et al., 2011. The mineralogy of late stage lunar volcanism as observed by the Moon Mineralogy Mapper on Chandrayaan-1. J. Geophys. Res. 116, E00G10.
Taylor, G.J., Warren, P., Ryder, G., Delano, J., Pieters, C., Lofgren, G., 1991. Lunar Rocks-Appendix: Chemical Data for Lunar Rocks. In: Lunar Source Book. Cambridge Univ. Press, Cambridge, UK, pp. 183–284.
Titley, S.R., 1967. Geologic map of the mare Humorum Region of the Moon. USGS Map I-495 (LAC-93), Scale:1:1,000,000.
Tompkins, S., Pieters, C.M., 1999. Mineralogy of the lunar crust: Results from Clementine. Meteorit. Planet. Sci. 34, 25–41.
Whitaker, E.A., 1972. Lunar color boundaries and their relationship to topographic features: A preliminary survey. Earth Moon Planets 4, 348–355.
Whitford-Stark, J.L., Head, J.W., 1977. The Procellarum volcanic complexes: Contrasting styles of volcanism. Proc. Lunar Planet. Sci. Conf. 8, 2705–2724.
Whitford-Stark, J.L., Head, J.W., 1980. Stratigraphy of Oceanus Procellarum basalts: Sources and styles of emplacement. J. Geophys. Res. 85, 6579–6609.
Wieczorek, M.A., Phillips, R.J., 2000. The 'procellarum kreep terrane' – Implications for mare volcanism and lunar evolution. J. Geophys. Res. 105, 20417–20430.
Wilhelms, D.E., McCauley, J.F., 1971. Geologic map of the near side of the Moon. USGS Map I-703, Scale 1:5,000,000.
Wilhelms, D.E., 1987. The Geologic History of the Moon. US Geological Survey Professional Paper (1348).
Williams, D.A., Greeley, R., Neukum, G., Wagner, R., Kadel, S.D., 1995. Multispectral studies of western limb and farside maria from Galileo Earth–Moon encounter 1. J. Geophys. Res. 100, 23291–23299.
Zhang, F., Zou, Y.L., Zheng, Y.C., Fu, X.H., 2012. Mapping homogeneous mare basalt units in the Aristarchus quadrangle using Clementine spectral parameters. Lunar Planet. Sci. Conf. 43, 1133 (abstract).
Zisk, S.H. et al., 1977. The Aristarchus–Harbinger region of the Moon: Surface geology and history from recent remote-sensing observations. Earth Moon Planets 17, 59–99.